Ref. Ares(2024)2906110 - 20/04/2024

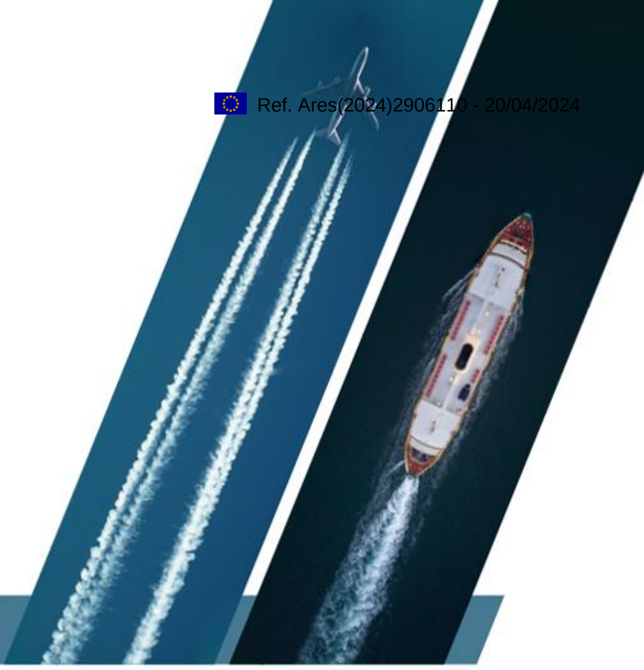

H2020-LC-SC3-2018-2019-2020
EUROPEAN COMMISSION
European Climate, Infrastructure and Environment Executive Agency (CINEA)

Biofuels production from **S**yngas
Fermentation for **A**viation and maritime use
Grant Agreement No 884208

Deliverable D6.4

Dynamic simulation and control of the BioSFerA process

Document Details

Due date	31/03/2024
Actual delivery date	20/04/2024
Lead Contractor	CERTH
Version	final
Prepared by	Christina Papaioannou, Anthi Plakia, Kostis Atsonios (CERTH)
Input from	Sakis Dimitriadis (CERTH)
Reviewed by	

Document Details

x	PU - Public
	PP - Restricted to other programme participants (including the EC)
	RE - Restricted to a group specified by the consortium (including the EC)
	CO - Confidential, only for members of the consortium (including the EC)

Disclaimer of warranties

This project has received funding from the European Union’s Horizon 2020 research and innovation programme under Grant Agreement No 884208. This document reflects only the author´s view and CINEA is not responsible for any use that may be made of the information it contains.

This document has been prepared by BioSFerA project partners as an account of work carried out within the framework of the EC-GA contract no 884208.

Neither Project Coordinator, nor any signatory party of BioSFerA Project Consortium Agreement, nor any person acting on behalf of any of them:

a. makes any warranty or representation whatsoever, express or implied,
    i. with respect to the use of any information, apparatus, method, process, or similar item disclosed in this document, including merchantability and fitness for a particular purpose, or
    ii. that such use does not infringe on or interfere with privately owned rights, including any party's intellectual property, or
    iii. that this document is suitable to any particular user's circumstance; or
b. assumes responsibility for any damages or other liability whatsoever (including any consequential damages, even if Project Coordinator or any representative of a signatory party of the BioSFerA Project Consortium Agreement, has been advised of the possibility of such damages) resulting from your selection or use of this document or any information, apparatus, method, process, or similar item disclosed in this document.

Contents

Executive Summary

This deliverable presents the dynamic simulation analysis of the BioSFerA main processes. A specific methodology for the development of the dynamic model was adopted and a strategy for the control of the key specification under various disturbances was built. For the plantwide control and the dynamic process simulation runs, the BioSFerA process was split into three parts, thermochemical, biological and thermocatalytic one and the analysis was performed separately.

For the thermochemical part, a Dual Fluidized Bed Gasification model that is exportable to Aspen Dynamics was developed in Aspen Plus. The model takes into account the hydrodynamics whereas the kinetic parameters of the main reactions were fine-tuned based in order to predict with good agreement the main products specifications as they have been reported in D6.2 for the large scale. The maintenance of the both reactors temperature and the syngas quality were the key conditions for the controllers setup.

The biological part of this deliverable presents a comprehensive dynamic simulation of syngas and acetate fermentation processes, designed for the continuous production of acetate and lipids, respectively. After fitting the model parameters using experimental and industrial-scale data, model validation for the industrial-scale data was conducted. Subsequently, the control systems for the validated model for both fermentation processes were integrated, using PID closed-loop controllers with feedback response mechanisms.

For the thermocatalytic part, an oil hydroprocessing model that is exportable to Aspen Dynamics was developed in Aspen Plus that includes both the fuel synthesis and recovery part. The model was verified against the respective data from the WP5 pilot activities. The control strategy was designed in such way that the reactor specifications (temperature, pressure and H_2/oil ratio) are maintained at the desired levels and the bio-jet fraction is recovered with the appropriate properties, targeting to boiling point.

1 Introduction

The present document encompasses the dynamic simulations of the three main sub-units (Dual Fluidized Bed Gasifier, Gas/Liquid Fermentation, TAGs hydroprocessing) of the BioSFerA concept. As initial point of reference, every investigated scenario was assumed to be in the steady state conditions presented in Deliverable D6.2 ‘Results of full-chain process simulations’. Dedicated unsteady conditions were applied in each sub-unit involving variations in feed streams flow rate and composition and changes in operating conditions. The dynamic simulations of the plant are carried out with the assistance of the commercial software Aspen Plus Dynamics^{TM} (APD) and Matlab/Simulink.

The main scope of the present dynamic study is the primary evaluation of the plant adaptability in targeted operational fluctuations and the identification of the required measures to achieve system restore according to the desired conditions. The present dynamic study is focused on the investigation of the concept flexibility in selected unsteady conditions, rather than the optimization of the applied control scheme and optimal dynamic response of the system. The latter could be investigated within the framework of a more in-depth dynamic analysis dealing with difficult situations (i.e. emergency scenarios) and assessing their techno-economic impact would require further maturation of the technology.

2 Approach and methodology

The dynamic behavior of each main sub-unit (Dual Fluidized Bed Gasifier, Gas/Liquid Fermentation, TAGs hydroprocessing) is investigated as well as their transition over different operational modes via an appropriate control scheme that ensures a continuously safe and efficient performance. The adaptability of the BioSFerA concept is assessed under different possible conditions.

The scope of this dynamic study is primarily the evaluation of the plant adaptability in operational fluctuations and the identification of the required measures to achieve system restore according to the desired conditions. The level of detail for each model is strongly depended on the available data from the respective pilot activities and the scale up approach for the design of the basic components.

It should be clarified that the main objective of the present dynamic study is limited to the investigation of the concept flexibility and adaptability in selected unsteady conditions, rather than the optimization of the applied control scheme and optimal dynamic response of the system. The latter along with the involvement of equipment failure situations can be re-evaluated with the further maturation of the technology.

3 Thermochemical part

3.1 DFBG – Steady state model and export to Aspen Dynamics

A 0.5D DFBG process model that is exportable to Aspen (Plus) Dynamics (APD) has been developed and validated. The model takes into account the basic geometrical aspects as are reported in D6.1 [1] and verified in T6.3, the reaction kinetic models that were also applied in D6.1 the hydrodynamics along the risers, the pressure drop in the whole dual system and the basic heat and mass balance information as have been reported in D6.2, downscaled to $100MW_{th}$ plant [2].

For the DFBG modeling, a different approach from that in D6.2 had to be adopted since the former model cannot be exported and executed in APD. Hence, a new DFBG model was developed in Aspen Plus^{TM} that is able to address the following three key challenges:

1. Overcoming the inherent weakness of APD for not supporting solids and inclusion of all the involved solids in the process i.e. fuel, sand and ash.

2. Inclusion of Reactor basic dimensions and hydrodynamics as they play important role on the process performance

3. Development of a model that is consistent with the former DFBG model as it was presented in D6.2 in respect of the heat and mass balance.

In order to overcome the above mentioned bottlenecks, the following assumptions – simplifications are necessary to be taken into account:

- Hydrodynamics mechanisms and phenomena that take place in a circulating fluidized bed such as the internal solids recirculation and the core-annulus effect are not taken into account.

- The heat losses at the reactors are calculated as 1% of the fuel heat input on a LHV basis

- Physical properties of the user defined 'solids' such as density and heat capacity (C_p) are constant and independent of the temperature.

3.1.1 Physical properties of the user defined solids

Table 1: Fuel stream composition (mol/mol)

Compound	Molar Composition
H_2O	0.0566
H_2	0.3202
O_2	0.1344
N_2	0.0012
S	0.0002
Char	0.4771
Ash	0.0103

A special approach is introduced for the modelling of the streams that are normally represented from non-conventional and solids compounds. This approach is based on the construction of user defined components C, ash (represented by the compound of Ca), permanent at liquid phase maintaining the properties (molecular weight,

H_{comb}, ρ, C_p, ΔH_{form}, ΔG_{form}) same to the corresponding real ones. As concerns the fuel stream, the feed stream that is considered is the devolatilized stream after the pyrolysis step. The composition of this stream is obtained from the model presented in Table 1.

As already mentioned, ash is modelled as an inert compound like Ca. The sand is considered as 50% $CaCO_3$ and 50% SiO_2 on a mass basis. Moreover, as the enthalpy of the feed stream is not the same with the enthalpy of the original ‘correct’ fuel, the energy balance consistency is satisfied by adding an inlet heat stream with the value of that difference. This value is obtained from the devolatilization reactor (RYIELD) of the D6.2 process model [2].

Following the same approach with the former DFBG process model (developed within D6.2), the remaining char is modelled as C instead of $C_aH_bO_c$.

For the definition of the user defined components (C, ash, $CaCO_3$, SiO_2), the main scope is to construct five components that will be permanently at the liquid phase (i.e. the extended Antoine vapor pressure to be equal to 0 and the normal boiling temperature to be very high) and will maintain all the physical properties of the real components (Table 2).

Table 2: User defined components physical properties.

Parameters	Units	C	ash	$CaCO_3$	SiO_2
Molecular weight	kg/kmol	12.01	40.08	100.09	60.08
Molar density	$kmol/m^3$	187.33	26.617	26.617	42.656
Ideal Gas Gibbs energy of formation	kJ/kmol	0	0	0	-307000
Ideal Gas Enthalpy of formation	kJ/kmol	0	0	-67400	229300
Heat of Vaporization	kJ/kmol	19.987	-	1.14 E+06	1.14 E+06
Ideal Gas Heat Capacity	J/kmol-K	38774	52907	83500	40900

3.1.2 Model description

Figure 1 presents a schematic depiction of the DFBG model as it was developed in Aspen Plus in the framework of the dynamic process simulations. It should be mentioned that all the sub-blocks along the Gasifier riser were modeled as continuous stirred tank reactors (CSTR). Although the most suitable reactor block to model the freeboard zone is the plug flow reactor (RPLUG), this was not allowed by Aspen Plus due to the minimum requirement for solid void fraction (>0.01). At first, a separator block (SEP) is employed to separate the components that formulate the fluid parts (volatiles and moisture) with the real solid one i.e. the ash and the C that corresponds to the fixed carbon (char).

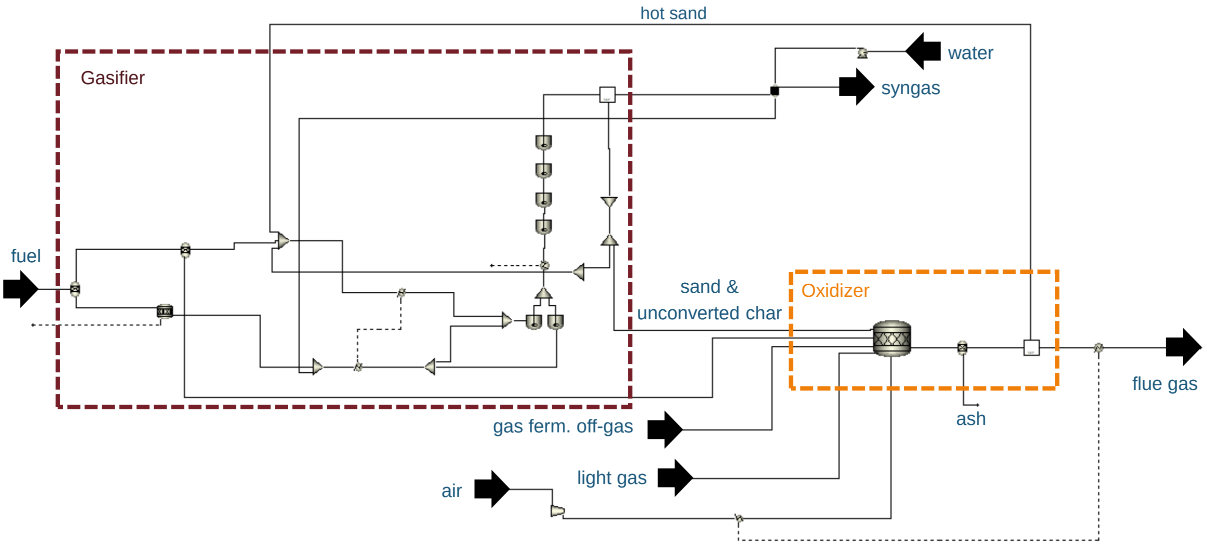

Figure 1. Aspen flowsheet of DFBG unit

3.1.3 Gasification reactions modeling

For the impurities, tars CO/CO_2 formation, the reactions in Table 3 are integrated in a RSTOIC:

Table 3: Reactions specifications for impurities formation (reactions occur in series)

	Fractional conversion	Fractional conversion of component	
$N_2 + 3H_2 \rightarrow 2NH_3$	0.8889	N_2	R 1
$2C+N_2+H_2 \rightarrow 2HCN$	0.0055	N_2	R 2
$C+2H_2 \rightarrow CH_4$	0.1712	C	R 3
$2C+2H_2 \rightarrow C_2H_4$	0.1367	C	R 4
$6C+3H_2 \rightarrow C_6H_6$	0.1021	C	R 5
$10C+4H_2 \rightarrow C_{10}H_8$	0.0881	C	R 6
$S + H_2 \rightarrow H_2S$	0.95	S	R 7
$2S + 2C + O_2 \rightarrow 2COS$	0.05	S	R 8
$Cl_2 + H_2 \rightarrow 2HCl$	1	Cl_2	R 9
$C+0.5O_2 \rightarrow CO$	0.7	C	R 10
$C+O_2 \rightarrow CO_2$	1.0	C	R 11

The fractional conversion rates were calculated by means of Calculator block targeting to approach the respective mole fractions of the impurities in the raw syngas, as they had been calculated and presented in D2.5 [3]. Moreover, the remaining C that does not take part in the HCs, HCN and COS formation is converted into CO and CO_2 by a ratio of 0.7/0.3.

In the gasification step, it is assumed that only homogeneous reactions (water gas shift R 12 and gas oxidation reactions R 13, R 14) take place in the bubble zone whereas in the emulsion zone both homogeneous and heterogeneous (water gas R 15 and Boudouard R 16) reactions are considered. Table 4 summarizes all the parameters for the gasification kinetic modeling. The homogeneous reactions were embedded straight at Aspen Plus as are first order Arrhenius whereas the kinetics for the heterogeneous were calculated via an external Fortran code.

Table 4. Gasification reactions kinetic parameters

No	Reaction	k	E (kJ/kmol)	Reaction expression (kmol/m³s)[1]	Ref
R 12	CO + H_2O ↔ CO_2 + H_2	222	12560	$r_{direct} = ke^{\left(-\frac{E}{RT}\right)}C_{CO}C_{H_2O}$	[4,5]
		2525.5	47290	$r_{reverse} = ke^{\left(-\frac{E}{RT}\right)}C_{CO_2}C_{H_2}$	
R 13	CO + $0.5O_2$ → CO_2	$5.779 \cdot 10^6$	125999	$r_{CO} = ke^{\left(-\frac{E}{RT}\right)}C_{CO}C_{O_2}^{0.5}C_{H_2O}^{0.25}$	
R 14	H_2 + $0.5O_2$ → H_2O	$1.08 \cdot 10^{13}$	124993	$r_{H_2} = ke^{\left(-\frac{E}{RT}\right)}C_{H_2}C_{O_2}$	
R 15	C + H_2O → CO + H_2	$239 \cdot 10^4$	129000	$r_{wat} = \frac{ke^{\left(-\frac{E}{RT}\right)}C_{H_2O}}{1 + K_{H_2O}C_{H_2O} + K_{H_2}C_{H_2} + K_{CO}C_{CO}}$ $K_{H_2O} = 3.16 \cdot 10^{-2}e^{\left(-\frac{30100}{RT}\right)}$ $K_{H_2} = 5.36 \cdot 10^{-3}e^{\left(-\frac{59800}{RT}\right)}$ $K_{CO} = 8.25 \cdot 10^{-5}e^{\left(-\frac{96100}{RT}\right)}$	
R 16	C + CO_2 → 2CO	$12.23 \cdot 10^{12}$	268000	$r_{bou} = \frac{ke^{\left(-\frac{E}{RT}\right)}C_{CO_2}}{1 + K_{CO_2}C_{CO_2} + K_{CO}C_{CO}}$ $K_{CO_2} = 6.6 \cdot 10^{-2}$ $K_{CO} = 12 \cdot 10^{-2}e^{\left(-\frac{25500}{RT}\right)}$	

[1] Molar concentrations are expressed in kmol/m³

The oxidizer reactor is modelled in a simpler way assuming that all combustibles totally react with the oxygen producing combustion products in a stoichiometric reactor (RSTOIC). The ash and the hot sand are perfectly removed from the flue gas after reactor exit while the latter one are led to the gasifier.

3.1.4 Hydrodynamics

A 1D model for fast fluidization is set aiming to calculate the particle distribution along the two risers [6]. Like in the majority of detailed CFB gasification process models in the literature, Kunii-Levenspiel model for circulating fluidized bed was employed [7],[8]. Information such as fluidization agent characteristics (U, μ), gas/solids density (ρ_g, ρ_p), particles mean diameter (d_p), reactor main dimensions (D, H_t, A_t), the gas distribution per nozzle (A_o) and total pressure drop (Δp), are used as input in order to calculate the bed height (H_{bed}), dense zone/ freeboard volume area, solid volume fraction distribution as well as the bubble/emulsion phase volume ratio (δ). The gasifier unit main design parameters are given in Table 5.

Table 5. Gasifier unit design and operational parameters

parameter	unit
reactor diameter, D (m)	3
reactor total height, H_t (m)	20
riser exit duct diameter, D_{red} (m)	1
downcomer length, L_{dc} (m)	13
loop seal height, h_{ls} (m)	0.5
loop seal length, L_{ls} (m)	0.5
loop seal depth, d_{ls} (m)	0.5
total inventory, W (kg)	20667
gas-distributor per nozzle, A_0 (m²/nozzle)	0.05

particles density, ρ_p (kg/m^3)	2500
hot syngas density - correcting factor of inlet gas density[1]	0.8
particles size diameter, d_p (μm)	159
gas viscosity, μ_g (Ns/m^2)	$38 \cdot 10^{-6}$

[1] the hydrodynamics calculations take place before the gasifier operation blocks and the current (syn)gas density is not yet available. To overcome that, it is considered that the gas density is the inlet gas density decreased by a certain correction factor

The superficial gas velocity U_0 is calculated as:

$$U_0 = 1.05 \frac{F_g}{\rho_g A} \qquad \text{Equation 1}$$

Where F_g is the gas inlet mass flow (in kg/s) and $A = 1/4 \cdot \pi \cdot D^2$ is the reactor cross flow area (in m^2).

The minimum fluidization velocity is calculated as:

$$U_{mf} = \frac{\left(\sqrt{{C_1}^2 + C_2 Ar} - C_1\right)\mu_g}{\rho_g d_p}, (C_1 = 27.2 \text{ and } C_2 = 0.0408) \qquad \text{Equation 2}$$

where Ar is the Archimedes number:

$$Ar = \frac{d_p^3 \rho_g (\rho_p - \rho_g) g}{\mu^2} \qquad \text{Equation 3}$$

The saturated solids diameter d_p^*:

$$d_p^* = d_p \left(\frac{g \cdot \rho_g \cdot (\rho_p - \rho_g)}{\mu^2} \right)^{1/3} \qquad \text{Equation 4}$$

Whereas the saturated gas velocity is:

$$U_g^* = U_0 \left(\frac{\mu_g \cdot g \cdot (\rho_p - \rho_g)}{\rho_g^2} \right)^{1/3} \qquad \text{Equation 5}$$

The solids entrainment velocity $U_{p,se}$ is:

$$U_{p,se} = 1.53 \sqrt{\frac{(\rho_p - \rho_g) d_p g}{\rho_g}} \qquad \text{Equation 6}$$

And the solid flux in the riser G_s (kg/m^{2}s) is:

$$G_s = \frac{F_{c,s}}{A} \qquad \text{Equation 7}$$

Where $F_{c,s}$ is the mass flow of the circulating solids.

The saturated terminal velocity is:

$$U_t^* = \frac{1}{\frac{18}{{d_p^*}^2} + \frac{0.591}{{d_p^*}^{0.5}}} \qquad \text{Equation 8}$$

and the terminal velocity U_t is calculated accordingly:

$$U_t = U_t^* \left(\frac{\mu (\rho_p - \rho_g) g}{\rho_g^2} \right)^{1/3} \qquad \text{Equation 9}$$

The saturated solids flux G_s^*:

$$G_s^* = 23.7\rho_p U_o exp\left(-5.5\frac{U_t}{U_o}\right)$$ Equation 10

And the saturation capacity of the gas is estimated based on the following equation:

$$\varepsilon_s^* = \frac{G_s^*}{(U_o - U_t)\rho_p}$$ Equation 11

For the hydrodynamics calculations at the dense zone, firstly it is estimated the fast fluidization input parameter alpha as

$$a = \frac{5}{U_o}$$ Equation 12

It is also assumed that the solid void fraction at dense zone is constant at $\varepsilon_{s,d}$ = 0.16. The solid void fraction at riser exit is estimated based on the following equation:

$$\varepsilon_{s,e} = \varepsilon_s^* + \left(\varepsilon_{s,d} - \varepsilon_s^*\right) \cdot exp(-a \cdot H_l)$$ Equation 13

where H_l is the total height of lean zone calculated as:

$$H_l = H_t - H_{bed}$$ Equation 14

The solid inventory at dense zone is:

$$W_{bed} = A \cdot \rho_p \cdot H_{bed} \cdot \varepsilon_{s,d}$$ Equation 15

The mean solid void fraction at lean zone is:

$$f = \varepsilon_s^* + \frac{\varepsilon_{s,d} - \varepsilon_{s,e}}{H_l \cdot a}$$ Equation 16

The solid inventory at lean zone is:

$$W_l = A \cdot \rho_p \cdot H_l \cdot f$$ Equation 17

Based on the above equations a corrected calculation of the lean zone height can be expressed from the following equation:

$$H_{l,new} = \frac{\frac{\varepsilon_{s,d} - \varepsilon_{s,e}}{a} + H_t \cdot \varepsilon_{s,d} - \frac{W}{A \cdot \rho_p}}{\varepsilon_{s,d} - \varepsilon_s^*}$$ Equation 18

The equations Equation 14 - Equation 18 are solved iteratively as soon the error e_{rr} = 1- $H_l/H_{l,new}$ becomes less than 0.0001.

In order to calculate the basic design characteristics in the dense zone (i.e. the volume of the emulsion and bubble phase zone) the following set of equations are used [9]. At first, the bubble diameter (d_b) is calculated from the following equation [10]:

$$d_b = 0.54\left(U_o - U_{mf}\right)^{0.4}\left(\frac{H_{bed}}{2} + 4\sqrt{A_o}\right)^{0.8} g^{-0.2}$$ Equation 19

The volume fraction of the bed consisting of bubbles (δ) is defined as:

$$\delta = \frac{U_{vis}}{U_{vis} - U_{b\infty}}$$ Equation 20

Where the single bubble velocity (u_b) is calculated as following [11]:

$$U_{b\infty} = 0.71(gd_b)^{1/2}$$ Equation 21

And the visible bubble flow:

$$U_{vis} = \psi\left(U_o - U_{mf}(1-\delta)\right)$$ Equation 22

$$\psi = \frac{0.26 + 0.70\cdot\exp\left(-3300d_p\right)}{\left(0.15 + U_o - U_{mf}\right)^{1/3}}\left(\frac{H_{bed}}{2} + 4\sqrt{A_o}\right)^{0.4}$$ Equation 23

The equations Equation 20 - Equation 23 are solved iteratively assuming an initial value for δ as soon the error e_{rr2} = 1- $\delta/\delta_{,new}$ becomes less than 0.0001.

The freeboard height is divided into four consecutive sub-regions with the same height (and consequently the same volume as the bed diameter is constant). The mean solid fraction at each sub-region is calculated according to the following equation:

$$\varepsilon_{s,l,i} = \varepsilon_s^* + (-\varepsilon_s^*)\cdot exp(-a\cdot H_i)$$ Equation 24

The pressure drop (in kPa) after both reactors at the dense zone is calculated as:

$$\Delta p_{d,i} = -\varepsilon_{s,d}H_d g\rho_p/1000$$ Equation 25

The pressure drop (in kPa) after each reactor at the lean zone is calculated as:

$$\Delta p_{l,i} = -\left(1-\varepsilon_{s,l,i}\right)H_i g\rho_p/1000$$ Equation 26

The pressure drop calculations for the rest part of the gasifier apart from the riser were based on the approaches of Karmakar and Datta [12] and Kaiser et al [13]. Firstly, the pressure drop at riser exit duct is calculated as [12]:

$$\Delta p_{red} = G_{red}\left(2.84 + 0.0108U_{red}^2\right)$$ Equation 27

where G_{red} is solid flux (kg/m^2-s) that based on the mass balance is:

$$G_{red} = G_s\frac{A}{A_{red}} = G_s\frac{A}{0.25\cdot\pi\cdot D_{red}^2}$$ Equation 28

and U_{red} the solids velocity (m/s):

$$U_{red} = \frac{G_{red}}{\rho_p}$$ Equation 29

The pressure drop at Cyclone is estimated as follows [13]:

$$\Delta p_{cyc} = k_{cyc} \rho_g U_0^2$$ *Equation 30*

where k_{cyc} is set equal to 30. For the downcomer, the voidage ε_{dc} is more than compact bed voidage, but less than voidage at minimum fluidization condition (ε_{mf}), so it is estimated as:

$$\varepsilon_{dc} = \delta_b + (1 - \delta_b)\varepsilon_{mf}$$ *Equation 31*

where the bubble fraction [13]:

$$\delta_b = \frac{1}{1 + \frac{1.3\left(0.15 + U_{ls} - U_{mf}\right)^{0.33}}{0.26 + 0.7e^{-3.3d_p}}\left(U_{ls} - U_{mf}\right)^{-0.8}}$$ *Equation 32*

and the voidance at the minimum fluidization velocity is set at $\varepsilon_{mf} = 0.5$. The velocity at loop seal (U_{ls}) is estimated according to the following relation:

$$U_{ls} = X_{ls} U_{mf}$$ *Equation 33*

The fluidization factor X_{ls} is between 5 and 10 and in this study it is set at 6. The pressure drop is then calculated as:

$$\Delta p_{dc} = -(1 - \varepsilon_{dc})\rho_p g L_{dc}$$ *Equation 34*

At the loop seal, there is a pressure drop at the standpipe and the horizontal part[13]:

$$\Delta p_{ls,st} = -(1 - \varepsilon_{dc})\rho_p g h_{st}$$ *Equation 35*

$$\Delta p_{ls,hor} = 3.5 \cdot \frac{U_{ls}}{2} \frac{A_{wall}}{A_{cross}} \rho_p \left(1 - \varepsilon_{mf}\right)$$ *Equation 36*

where $A_{wall} = 2 \cdot L_{ls}(h_{ls} + d_{ls})$ and $A_{cross} = L_{ls} \cdot d_{ls}$

3.2 Model verification and sensitivity analysis

The main operating conditions are presented in Table 6.

Table 6. Main operating conditions for the thermochemical part of the BioSFerA concept

Parameter	Input
Pressure (bar)	1.5
Gasifier temperature (°C)	780
Oxidizer temperature (°C)	880
Steam-to-biomass ratio (kg/kg dry,ash free)	0.7
Steam pre-heating temperature (°C)	350
Air pre-heating temperature (°C)	400
Pressure drop in the gasifier (bar)	0.2

Table 7 compares some of the main simulation results from the process models developed in Task 6.2 and here. The small relative errors in all parameters indicate that both models are in good agreement and allow the use of the latter for the dynamic simulation analysis.

Table 7. Dynamic DFBG model validation

		D6.2 model	D6.4 model	rel. error
gasifier temperature outlet	^{o}C	780	774	-0.8%
syngas flow	Nm^3/h	36753	36930	0.5%
unconverted char	kg/h	1340	1394	3.9%
raw syngas composition				
H_2O	v/v	32.5%	30.3%	-7.4%
H_2	v/v	31.6%	33.5%	5.8%
CO	v/v	13.4%	12.2%	-9.9%
CO_2	v/v	14.6%	16.2%	9.6%
CH_4	v/v	5.3%	5.3%	-0.5%
C_2H_4	v/v	1.8%	1.8%	-0.5%
tars	v/v	0.6%	0.6%	-0.5%
NH_3	v/v	0.2%	0.2%	-0.5%
N_2	ppm	115.0	119.8	4.0%
H_2S, HCN, COS	ppm	202.4	180.8	-12.0%

Figure 2 demonstrates how the voidance, reactor temperature, main syngas products composition and pressure evolves along the gasification riser. The last graph shows the pressure drop not only at the riser but also at the return system. The temperature is almost stable along the dilute zone whereas it is seen that the WGS reactor prevails at this region.

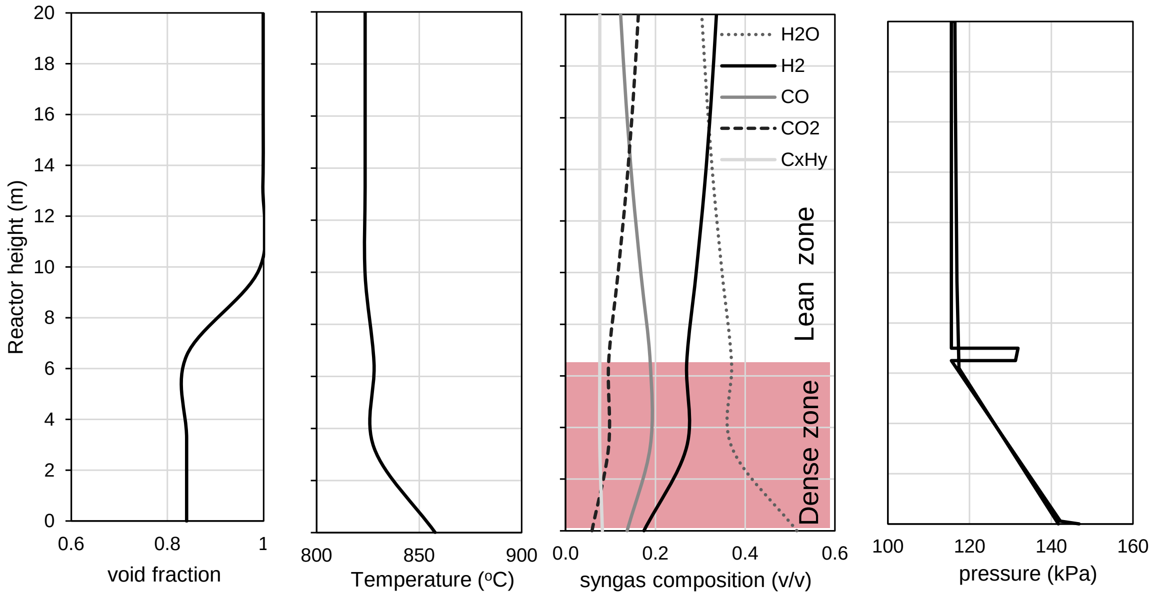

Figure 2. Steady state simulation results along the gasifier riser (the last graph depicts the pressure drop at the riser and return system as well)

Several parametric investigations have been carried out in order to identify the most important and critical parameters, the change of which affect the performance and operation of the DFBG unit. Indicatively, Table 8 demonstrates how the exclusion of one of both combustibles gases (“Ext gas”: the light gas coming from the fractionation unit after hydrotreatment, “Ferm gas”: off gas after the gas fermenter) that are burnt in the oxidizer affects the overall process operation. As great variance in several parameters such syngas quality and composition is observed due to the necessary change in the flow of unconverted char, two of the examined scenarios will be to control the unit when the normal feed of these streams fail.

Table 8. Influence of external combustible gas streams on process operation

	base case	Ext gas = 0	Ferm gas = 0
Circulating solids inlet temp (ºC)	880	880	880
syngas Flow (kg/s)	8.50	8.45	8.28
syngas LHV (MJ/kg)	10.91	10.71	10.05
syngas heat input (MW_{th})	92.67	90.49	83.23
Syngas outlet temp (ºC)	773.8	767	739.5
Circulating solids flow (t/h)	451.9	392.9	242.9
Unconverted char flow (t/h)	1.40	1.57	2.17
H_2O	30.3%	31.4%	35.7%
H_2	33.5%	33.0%	30.7%
CO	12.2%	11.4%	8.7%
CO_2	16.2%	16.4%	16.7%
H_2/CO	2.75	2.90	3.53

The following graphs show the impact of the operating pressure of the gasifier, as it is illustrated by the steam inlet pressure, on the syngas composition and quality:

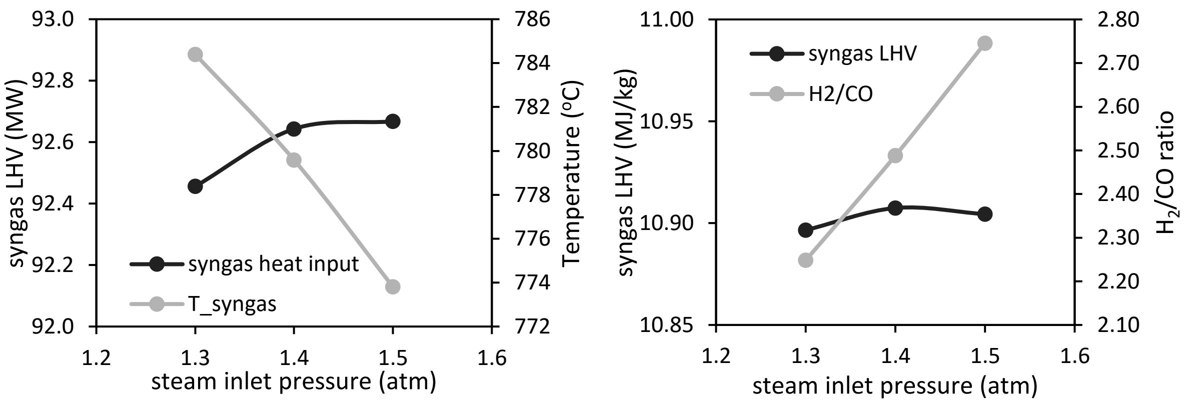

Figure 3. Impact of gasifier pressure on produced syngas quality and composition

The increase in steam pressure inlet causes the lowering of the gasification temperature (autothermal conditions) and increase in H_2/CO ratio that may have direct impact on the gas fermentation operation.

The Aspen Plus model has been successfully exported to Aspen Plus Dynamics and is able to run at steady state (for the time being) with no errors or problems (see Figure below).

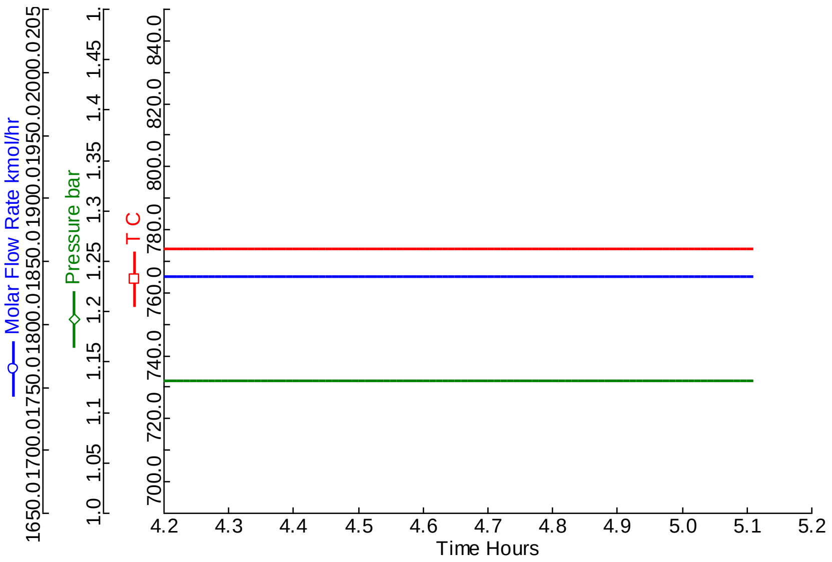

Figure 4. Temporal evolution of syngas main characteristics at stable conditions

3.3 Control strategy and examined scenarios

The following table summarizes the scenarios and the respective control strategies that are going to be investigated at dynamic/unsteady conditions:

Table 9. Examined scenarios and the control strategy (tentative)

a/a	Disturbance/change	Target	Variable parameter(s)
1	Change in feedstock flow rate	Keep syngas quality and temperature	Steam flow Circ. Solids flow Air flow
2	Decrease in steam flow	Keep H_2/CO ratio	Circ. Solids flow Air flow
3	Decrease in gasification temperature	Keep H_2/CO ratio and S/C ratio	Steam flow Circ. Solids flow Air flow
4	External combustible gas cut-off	Keep H_2/CO ratio	Circ. Solids flow Steam pressure outlet

Before the run of the examined scenarios, the controllers are tuned in order to operate properly. The set point (SP), process variable (PV) and the operating parameter (OP) of each controller are seen in Figure 5whereas their respective specifications after tuning are summarized in Table 10. All controllers are PI.

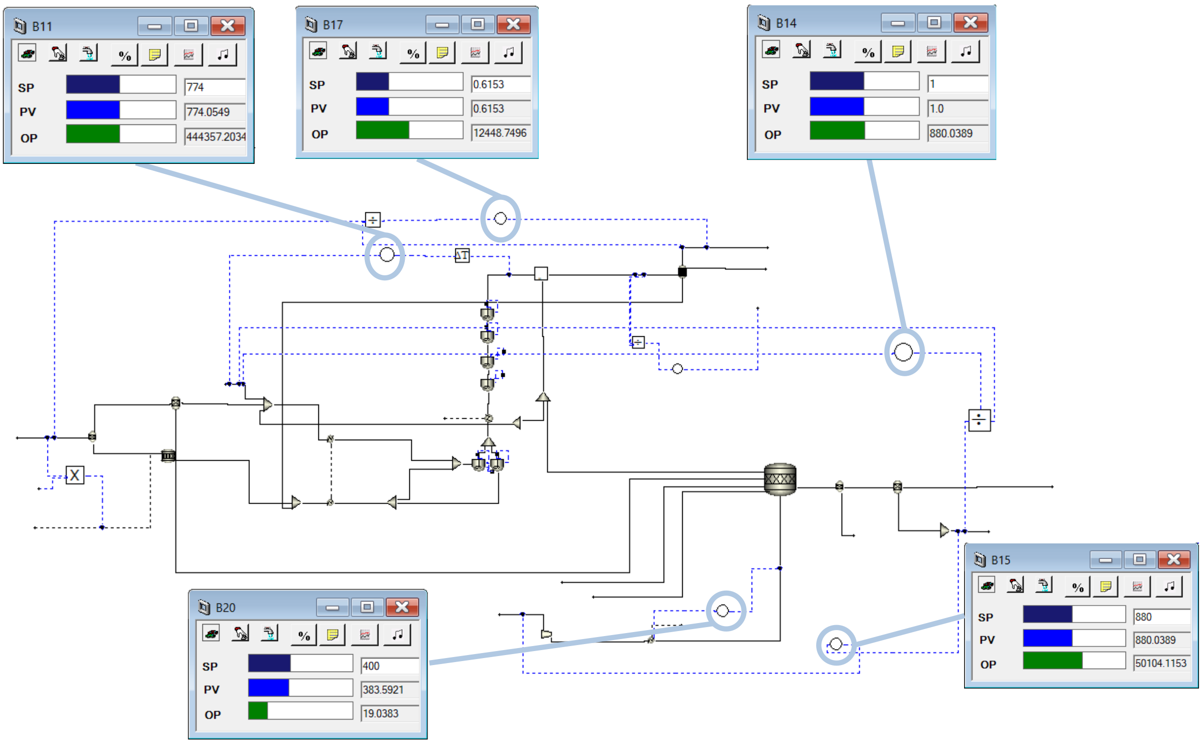

Figure 5. Aspen Plus Dynamics process flowsheet and controllers parameters

Table 10. DFBG model controllers specifications

Controller Name (Figure 5)	Gain (%/%)	Integral time (min)	Controller action	Tuning rule
B11	37.120853	2.070875	Reverse	IMC
B17	1.829	1.997714	Reverse	IMC
B14	1	20	Direct	IMC
B15	3.143166	1.08564	Reverse	IMC
B20	1	20	Reverse	IMC

3.4 Dynamic simulations

3.4.1 Feedstock flowrate

In this scenario, the step change of feedstock flow through sudden decrease and increase is investigated. At first, the biomass flow rate drops by 20% and after 2 hours, it decreases again by 20% operating for 1.5h at 60% load. Then, the full load operation is restored (see Figure 6 blue line). The circulating solids flow (Figure 6 grey line) is the process variable to keep the gasification temperature stable (set point) and its variation has strong similarities with that of syngas temperature (Figure 7 blue line). It is observed that the syngas temperature restoration is accomplished with half an hour at all changes occurred. On the other hand, since the circulating solids flow is pretty large, no temperature change is observed.

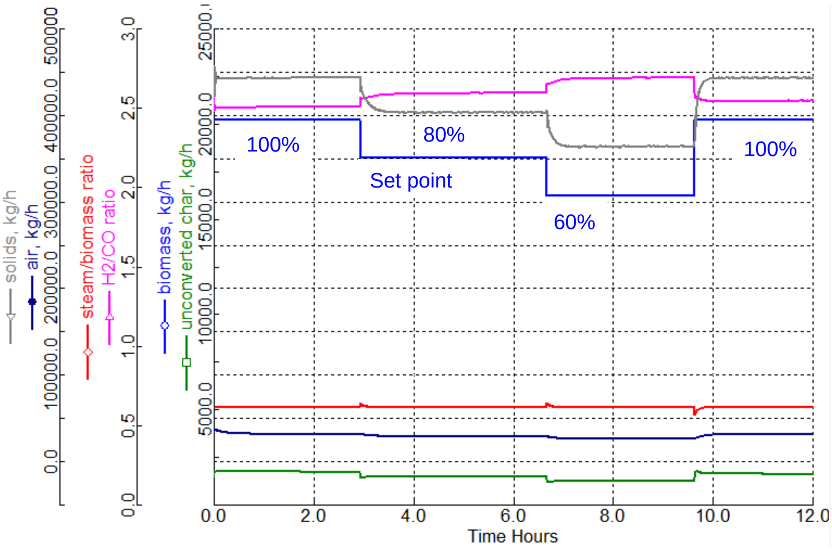

Figure 6. Evolution of DFBG operation parameters at load variations

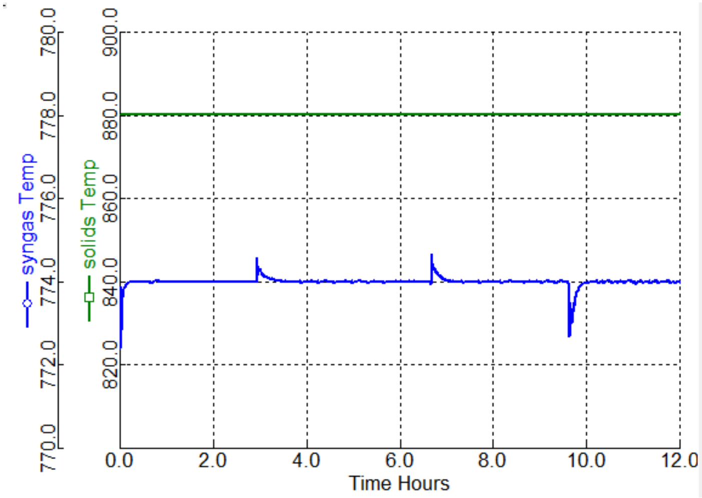

Figure 7. Reactors temperature evolution

It takes around 30 min to restore the temperature level at the gasifier. On the contrary, the temperature at the oxidizer remains the same along the whole time period, as illustrated from the hot sand temperature. This is attribute to the large mass flow and the high heat capacity of the solids that does not favor the great temperature variations.

What is also observed and should be mentioned is that during the period that the DFBG operates at lower load the H_2/CO increases, changing the syngas quality that exit the gasifier. In case that this variation has negative effect on gas fermentation performance and in case that the steam catalytic reforming that follows the gasification process is not at the position to restore the syngas composition at the initial desired level, an alternative control strategy should be adopted.

3.4.2 Steam flow rate

For this scenario, the temporal variation of inlet water/steam that is illustrated by the steam to biomass ratio is seen in red in Figure 8 (left). It was also observed that both the gasification and combustion process operate at the same temperatures without variation. To achieve that, the circulating solids flow and the unconverted char flow vary considerably. The control scheme operates in such a way that the H_2/CO ratio almost remains constant at around 2.5. In other words, this control approach is appropriate to keep the syngas quality at a stable and desired level.

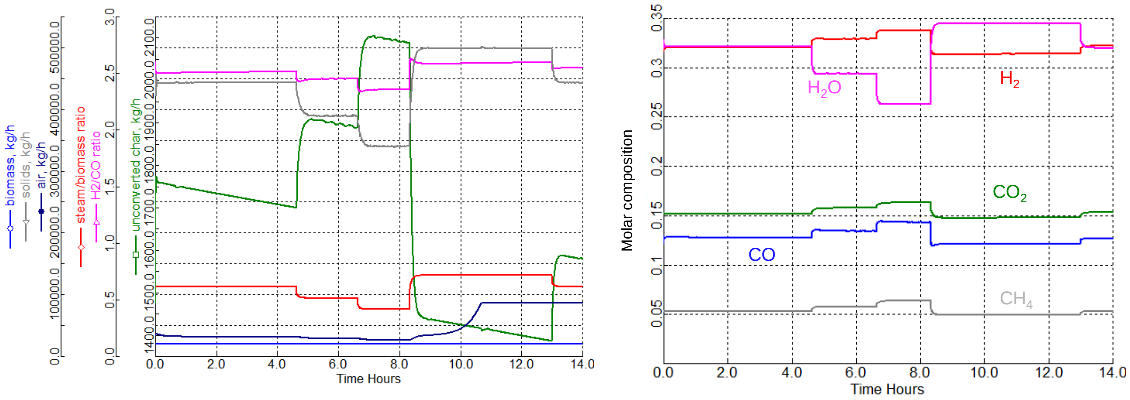

Figure 8. Effect of various DFBG process parameters on steam flow variation

3.4.3 Gasifier temperature

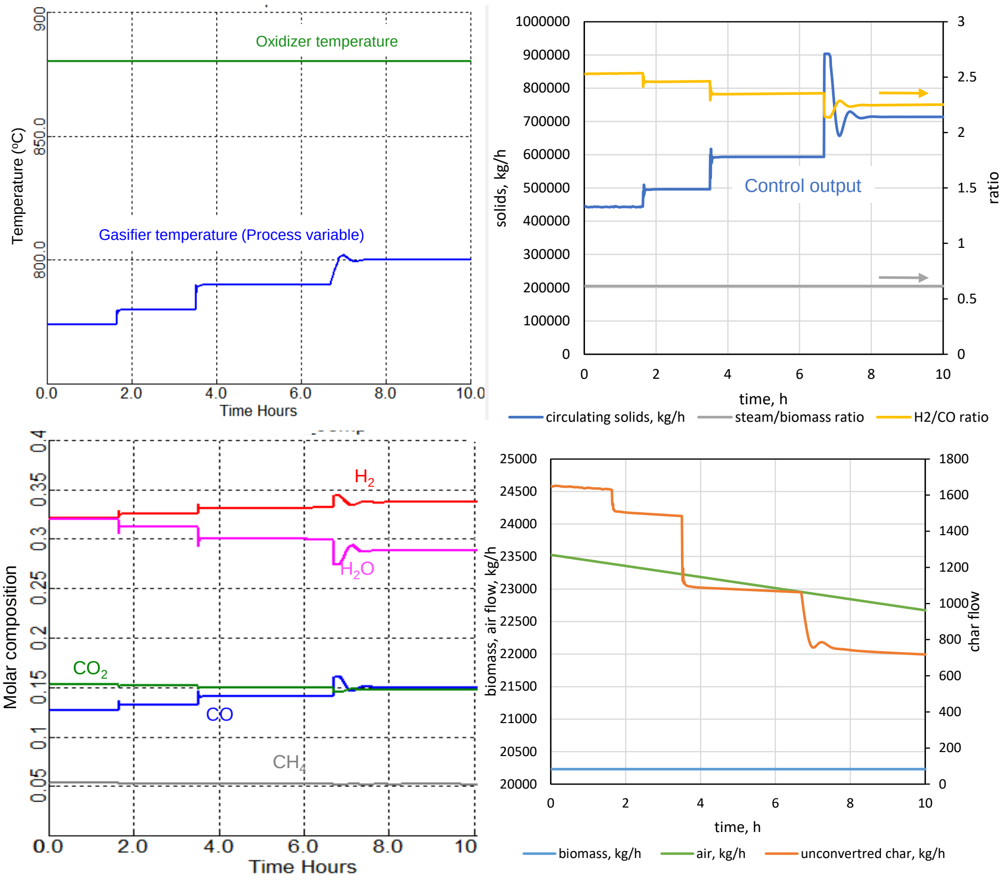

Figure 9. Effect of various DFBG process parameters on gasifier temperature variation

In this section, the sudden change (increase) of gasifier temperature up to 800 °C in three steps is examined. Like in other cases, the oxidizer (or hot sand) temperature remains the same during the whole test run. To achieve that, the solids (hot sand) circulation flow should have been controlled properly. The char conversion at the gasifier increases as gasifier temperature gets higher, then the unconverted char drops and the circulating solids (control output) should increase in order to cover the elevated heat demands at the gasifier. The hydrogen and CO content in the syngas increases probably due to the higher conversions in water gas reaction (R 15) and thus the H_2/CO ratio does not vary considerably.

3.4.4 Fermentation off gas flow

Figure 10 shows how the main process parameters are affected from the change (sudden stop) of fermentation off gas flow rate. When this occurs, the main operation temperatures (i.e. gasification and hot sand) cannot maintain at their initial levels and drop. The unconverted char that increases is not sufficient enough to restore them. As a matter of that, the produced syngas decreases and the H_2/CO increases because the WGS reaction favors from the fact that more steam is available to react with CO as carbon water gas reaction rate decreases.

It should be mentioned that the control scheme in that case is set up in such way that the recirculating solids flow rate and steam to biomass ratio remain unstable. In case that the change in syngas composition does not favors the gas fermentation efficiency, an alternative control strategy should be established.

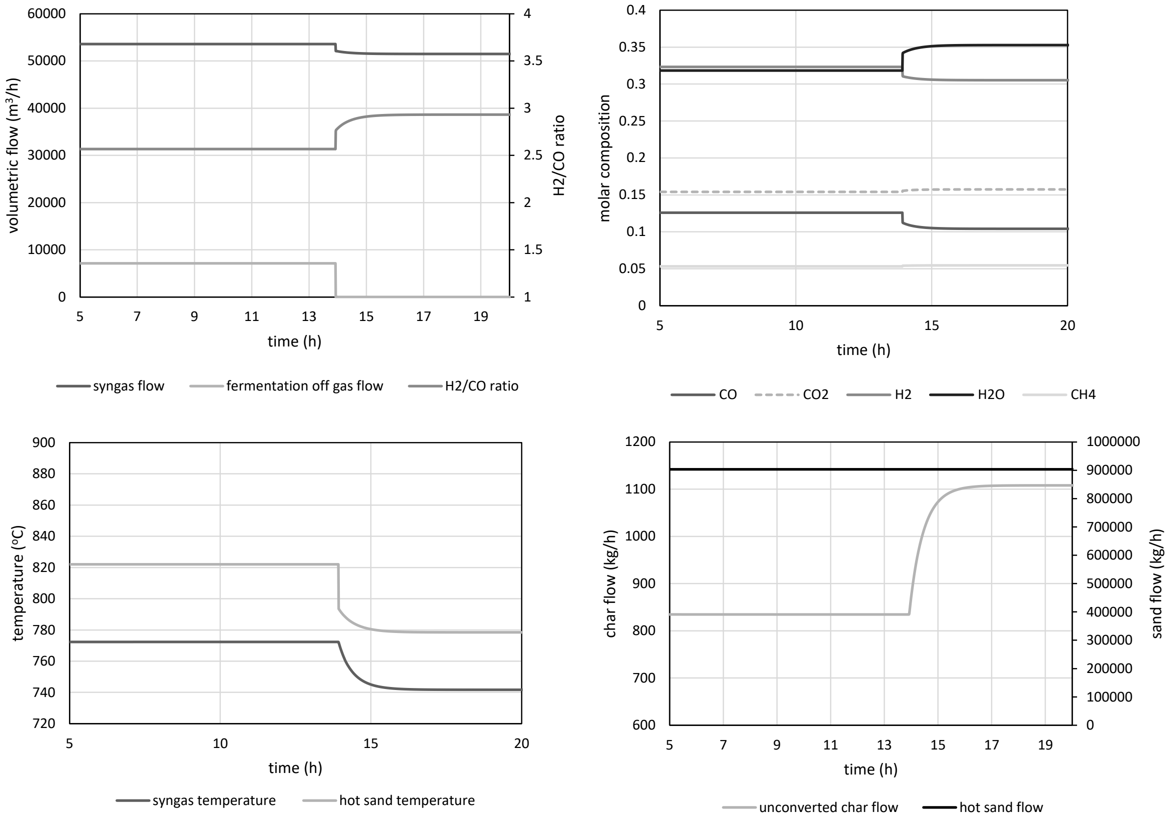

Figure 10. Effect of fermentation off gas flow on DFBG parameters

4 Biological part

The aim of this section is to conduct dynamic simulations for the biological part of the system and to design a plant-wide control system to regulate syngas composition in accordance with strain specifications while minimizing by-products. The biological part consists of two different fermentation processes: syngas fermentation and acetate fermentation. In the first one, which involves the gaseous substrate, syngas is converted into acetate under anaerobic conditions using advanced acetogenic bacteria. The acetyl-CoA pathway, also known as the Wood-Ljungdahl pathway, can utilize both CO and H_2 as electron donors and CO and CO_2 as carbon sources (Figure 11).

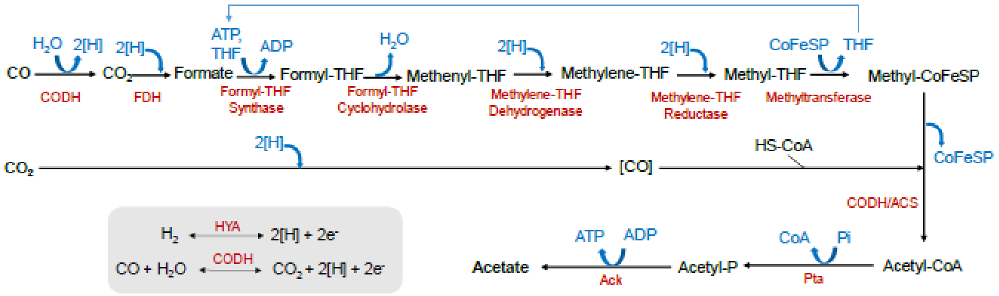

Figure 11: Wood-Ljungdahl Pathway for acetate synthesis from CO/CO2/H2 syngas

The chemical reactions catalyzed by the cell are presented in R 17 and R 18:

$$4\ CO + 2\ H_2O \rightarrow C_2H_4O_2 + 2\ CO_2 \qquad \text{R 17}$$

$$4\ H_2 + 2\ CO_2 \rightarrow C_2H_4O_2 + 2\ H_2O \qquad \text{R 18}$$

In the second fermentation step, which involves the liquid substrate, the produced acetate is converted into targeted lipids, namely triacylglycerides (TAGs), under aerobic conditions, using oleaginous yeasts such as *Yarrowia lipolytica*. The metabolic model depicting this process is illustrated in Figure 12.

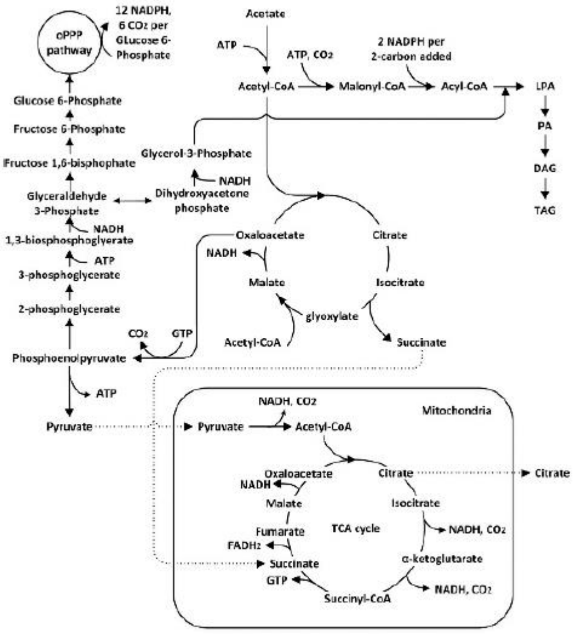

Figure 12: Reaction mechanism for TAGs production through acetate fermentation

There are two steps involved in this process, the growth phase and the lipid production phase. In the growth phase, biomass must be generated for the yeasts to accumulate lipids. The stoichiometric equation for this phase is expressed by R 19.

$$CH_3COOH + 0.908\ O_2 + 0.147\ NH_3 \rightarrow 1.05\ CH_{1.66}O_{0.54}N_{0.14} + 1.349\ H_2O + 0.95\ CO_2 \qquad \text{R 19}$$

In the second phase, lipids are produced inside the cultivated yeasts. The stoichiometric equation for this phase is presented in R 20.

$$50.11\ CH_3COOH + 27.72\ O_2 \rightarrow C_{51}H_{98}O_6 + 51.22\ H_2O + 49.22\ CO_2 \qquad \text{R 20}$$

This section focuses on the dynamic simulation of the industrial-scale implementation of the two fermentation processes. The suggested double-stage fermentation scheme for the scale up is depicted in Figure 13.

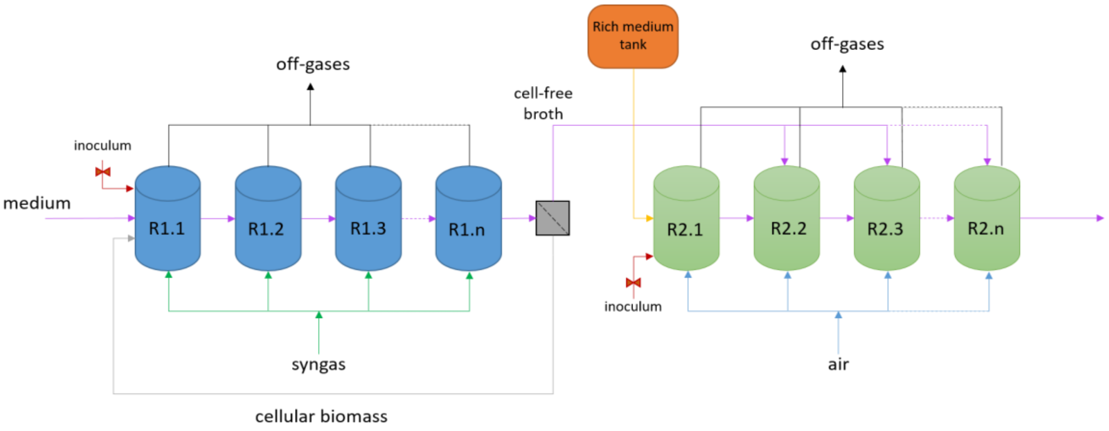

Figure 13: Suggested double-stage fermentation scheme for the scale up

More particularly, in the gas fermentation process, syngas, that is the substrate, is distributed among 30 bioreactors and enters the bioreactors in parallel. The liquid medium is fed in series from the first bioreactor stage to downstream stages [14]. The acetate concentration gradually increases in the bioreactors, and the final concentration must reach up to 30 g/L to prevent accumulation.

For the liquid fermentation process aimed at TAGs production, two phases are considered. The first phase involves a CSTR reactor serving as the biomass growth phase in a rich medium under continuous and aerobic conditions. The second phase is dedicated to TAGs production, operating under continuous and nitrogen-limited conditions. In this phase, the acetate previously produced is divided among 29 reactors and added in parallel. Additionally, air is added in parallel in both phases. Cells are harvested at the outlet of the final stage [15].

4.1 Dynamic process simulation

Based on the analyzed scale-up scheme, a mathematical model is developed using MATLAB and Simulink for dynamic process simulation. Firstly, the differential equations for mass balances are determined based on the biological reactions of each fermentation process. Two phases, gas and liquid, are considered, and the differential equations for components are derived according to their respective phases.

In the dynamic model, several kinetic parameters must be determined using MATLAB's optimization tool "fmincon". Firstly, for the syngas fermentation process, the kinetic parameters are fitted to the experimental data for cleaned syngas from D3.4 [16] and then to the experimental data from T4.3 when syngas is contaminated with impurities. For the acetate fermentation process, the kinetic parameters are fitted to the experimental data from D3.5 [17].Then, based on the industrial-scale data from D6.2 [2], the final fitted parameters for each case are found.

Once the kinetic parameters for the industrial-scale data from D6.2 [2] are fitted, the dynamic simulation is developed in Simulink, and validated by achieving the similar final product concentration with D6.2 [2]. Both fermentation processes are assumed to operate continuously in bioreactors. Feed is added while product is withdrawn, treating the bioreactors as simple continuous stirred tank reactors (CSTRs) where various biological reactions take place. Assumptions include perfect mixing within the reactor, constant pH, and constant flow rates for substrate feed and product output.

Subsequently, a plant-wide control system is developed for both syngas and acetate fermentation. The objective for syngas fermentation is to control acetate concentration by adjusting the agitation speed in response to changes in syngas composition. For acetate fermentation, the substrate flowrate is the varying parameter that affects the final TAGs concentration and acetate residual. By manipulating the biomass concentration produced in growth phase -by adjusting the C/N ratio, oxygen flowrate and agitation speed- the final acetate concentration is controlled to the desired value that must be close to zero.

The following sections, 4.1.1 and 4.1.2, describe the dynamic simulation of the two fermentation processes in detail.

4.1.1 Syngas Fermentation

4.1.1.1 Model description and parameter fitting

Mass balance equations:

As previously described, the dynamic model for syngas fermentation occurs in a continuous stirred tank reactor (CSTR). The components are divided into non-condensable and condensable and they exist either in liquid or gas phase. The differential equations, Equation 37-Equation 41, assume isothermal and isobaric operation, as well as homogeneity and constant liquid and gas volumes in the reactor [18].

For non-condensable components, j, that are CO, H_2, CO_2, and the impurities NH_3, H_2S, HCN, COS, Benzene:

In the gas phase:

$$\frac{dC_{G,j}}{dt} = \left(\frac{1}{V_G}\right)\left(Q_{G,in} \cdot C_{G,j,in} - Q_{G,out} \cdot C_{G,j}\right) - k_L a_j \left(\frac{C_{G,j}}{m_{j,NC}} - C_{L,j}\right)\left(\frac{V_L}{V_G}\right)$$

Equation 37

In the liquid phase:

$$\begin{aligned} For\ CO, H_2, CO_2{:}\ \frac{dC_{L,j}}{dt} &= \left(\frac{Q_L}{V_L}\right)\left(C_{L,j,in} - C_{L,j}\right) + k_L a_j \left(\frac{C_{G,j}}{m_{j,NC}} - C_{L,j}\right) + v_j \cdot C_X \\ For\ impurities{:}\ \frac{dC_{L,j}}{dt} &= \left(\frac{Q_L}{V_L}\right)\left(C_{L,j,in} - C_{L,j}\right) + k_L a_j \left(\frac{C_{G,j}}{m_{j,NC}} - C_{L,j}\right) \end{aligned}$$

Equation 38

For condensable components, j, that are acetate, H_2O:

In the gas phase:

$$\frac{dC_{G,j}}{dt} = \left(\frac{1}{V_G}\right) \cdot \left(Q_{G,in} \cdot C_{G,j,in} - Q_{G,out} \cdot C_{G,j}\right) + k_L a_j \left(\frac{C_{L,j}}{m_{j,C}} - C_{G,j}\right)\left(\frac{V_L}{V_G}\right)$$

Equation 39

In the liquid phase:

$$\frac{dC_{L,j}}{dt} = \left(\frac{Q_L}{V_L}\right) \cdot \left(C_{L,j,in} - C_{L,j}\right) - k_L a_j \left(\frac{C_{L,j}}{m_{j,C}} - C_{G,j}\right) + v_j \cdot C_X$$

Equation 40

For the biomass concentration, C_X, in the liquid phase:

$$\frac{dC_X}{dt} = \left(\frac{Q_L}{V_L}\right)\left(-C_X \cdot XP\right) + \mu \cdot C_X - r_d$$

Equation 41

Where $m_{j,NC}, m_{j,C}$ parameters are the gas-liquid equilibrium factors for non-condensable and condensable components, listed in Annexes.

The industrial-scale fermentation consists of 30 CSTR, where V_G, V_L, are the volumes of gas and liquid inside each reactor and equal to 50000 L and 250000 L, respectively. The volumetric flow rate in, $Q_{G,in}$, and out, $Q_{G,out}$, of the reactor are both at $656043\,\frac{L}{hr}$, and $XP = 0$, meaning that all cells are recycled to the reactor. The above values are obtained from D6.2 [2].

Reaction rates:

The specific consumption/production rates of species CO and H_2 , $v_{CO,\ H2}$ $\left(\frac{mol}{g \cdot hr}\right)$ are estimated in Equation 42 [18]:

$$v_{CO,\ H2} = -\frac{v_{max,j} C_{L,j}}{K_{S,j} + C_{L,j}} I_i I_{CO}$$

Equation 42

Where i are the Acetic acid, NH_3, H_2S, HCN, COS, Benzene components, and $I_i = \frac{1}{1 + \frac{C_{L,i}}{K_{I,i}}}$, $I_{CO,j=H_2} = \frac{1}{1 + \frac{C_{L,CO}}{K_{I,CO}}}$, $I_{CO,j=CO} = 1$.

The specific biomass growth rate $\mu\ (hr^{-1})$ is calculated from these rates and yield coefficients $Y_{X,CO}$ and $Y_{X,H2}$, Equation 43:

$$\mu = -v_{CO} Y_{X,CO} - v_{H2} Y_{X,H2}$$

Equation 43

The death rate r_d is a function of cell concentration, as shown in Equation 44:

$$r_d = k_d C_X$$ Equation 44

where k_d is the death constant.

The reaction rates from Reactions 1 and 2 are calculated from Equation 45 and Equation 46:

$$v_{1R} = -\frac{v_{CO}}{4}$$ Equation 45

$$v_{2R} = -\frac{v_{H2}}{4}$$ Equation 46

The total consumption/production rates of other components are calculated from Equation 47- Equation 49:

$$v_{CO2} = 2v_{1R} - 2v_{2R}$$ Equation 47

$$v_{HAc} = v_{1R}Y_{AcCO} + v_{2R}Y_{AcH2}$$ Equation 48

$$v_{H2O} = -2v_{1R} + 2v_{2R}$$ Equation 49

So, the unknown kinetic parameters that are estimated are the k_d, the yield coefficients used in these calculations, $v_{max,CO}$, $v_{max,H2}$, $K_{S,j}$, $K_{I,j}$.

Mass transfer coefficients:

To calculate the mass transfer coefficients k_La_j several equations must be determined based on literature [18]. Firstly, the mass transfer coefficient k_La for air in water at 20 ºC is described by Equation 50:

$$k_La^{(20)}(hr^{-1}) = f_0 k_La_0^{(20)} + (1 - f_0)k_La_1^{(20)}$$ Equation 50

Where $k_La_0^{(20)}$ and $k_La_1^{(20)}$ are the nonalescing and coalescing broth according to the correlations proposed by van't Riet (1979) for air in water and are described by Equation 51 and Equation 52, respectively:

$$k_La_0^{(20)}(hr^{-1}) = 3600(0.002\left(\frac{P_g}{V_L}\right)^{0.7}(u_s)^{0.2}$$ Equation 51

$$k_La_1^{(20)}(hr^{-1}) = 3600(0.026\left(\frac{P_g}{V_L}\right)^{0.4}(u_s)^{0.5}$$ Equation 52

Where u_s, is the superficial gas velocity and $\frac{P_g}{V_L}$ is the impeller power per unit volume, which is estimated from the impeller ungassed power P_{ug} (Equation 53) and the correlation for the P_g in Equation 54.

$$P_{ug} = N_p \rho_L N^3 d_i^5$$ Equation 53

$$\frac{Q_{G,in}N^{0.25}}{d_i^2} \leq 0.055 \rightarrow P_g = -(9.9\left(\frac{Q_{g,in}N^{0.25}}{d_i^2}\right)P_{ug} - P_{ug})$$
$$\frac{Q_{G,in}N^{0.25}}{d_i^2} \geq 0.055 \rightarrow P_g = -(0.52 + 0.62\left(\frac{Q_{g,in}N^{0.25}}{d_i^2}\right)P_{ug} - P_{ug})$$ Equation 54

The ungassed power number, N_p, is described by [19] for 1 impeller, Equation 55:

$$N_p = Agspeed^3(39.3701 \cdot d)^5(4.5 \cdot 10^{-13})$$ Equation 55

Where $Agspeed$ is the agitation speed in rpm, and $N(s^{-1}) = 0.01667 \cdot Agspeed$

In all cases, it is assumed that the reactor has a Height/Diameter ratio of 3 and an impeller diameter, d, of 40% the reactor diameter, D.

The mass transfer coefficient at different temperature is expressed by Equation 56:

$$k_L a^{(T)}(hr^{-1}) = \frac{k_L a^{(20)}}{1.024^{(20-T)}}$$ Equation 56

The individual $k_L a_j$ for each component is calculated by Equation 57, by applying the penetration theory:

$$k_L a_j = k_L a^{(T)} \left(\frac{D_{f,j}}{D_{f,air}}\right)^{\frac{1}{2}}$$ Equation 57

Where $D_{f,j}$ is the mass diffusivity of species j in water and are expressed in Annexes. Based on the above, the unknown parameters that are estimated are the weighting factor, f_0 and the agitation speed.

Estimation of model parameters:

The unknown parameters expressed above, that are the k_d, the yield coefficients, $v_{max,CO}$, $v_{max,H2}$, $K_{S,j}$, $K_{I,j}$, f_0, AgSpeed are estimated using the maximum likelihood principle (MLP), [18], with data retrieved from experimental data from D3.4 [16] for cleaned syngas, then from experimental data from T4.3 for syngas with impurities and finally from industrial-scale data from D6.2 [2], that are these being used in the dynamic simulation. The fitted parameters and the dynamic profile of each case are illustrated in Annexes. Given the high nonlinearity of the MLP method, the objective function is minimized using the “fmincon” function in MATLAB. This approach ensures a good initial estimation of parameters, enhancing the accuracy of the MLP results.

Model simulation:

After the kinetic parameters are fitted to the industrial scale data, the syngas fermentation process is simulated in Simulink and its results are compared against those from D6.2 [2], to validate the model. The dynamic syngas fermentation model is a nonlinear algebraic-differential system, demanding numerical solvers suitable for stiff problems. Therefore, the ode15s method from MATLAB is used for time integration from the initial conditions based on D6.2 [2]. The initial feedstock and operating conditions are outlined in Table 11.

Table 11: Initial feedstock and operating conditions

Syngas composition (mol/L)	
CO	0.043
H_2	0.077
CO_2	0.024
NH_3	0.000019
H_2S	0.0000089
HCN	0.0000003
COS	0.0000017
Benzene	0.000005
$Q_{g,in}$ (L/h)	656044
Operating conditions	
Temperature (°C)	55
Pressure (bar)	5
$Q_{l,in}$ (L/h)	848629

The Simulink model, depicting two of the thirty reactors for syngas fermentation, is illustrated in Figure 14 and Figure 15. These figures provide a visual representation of the setup and operation of the fermentation process within the reactors.

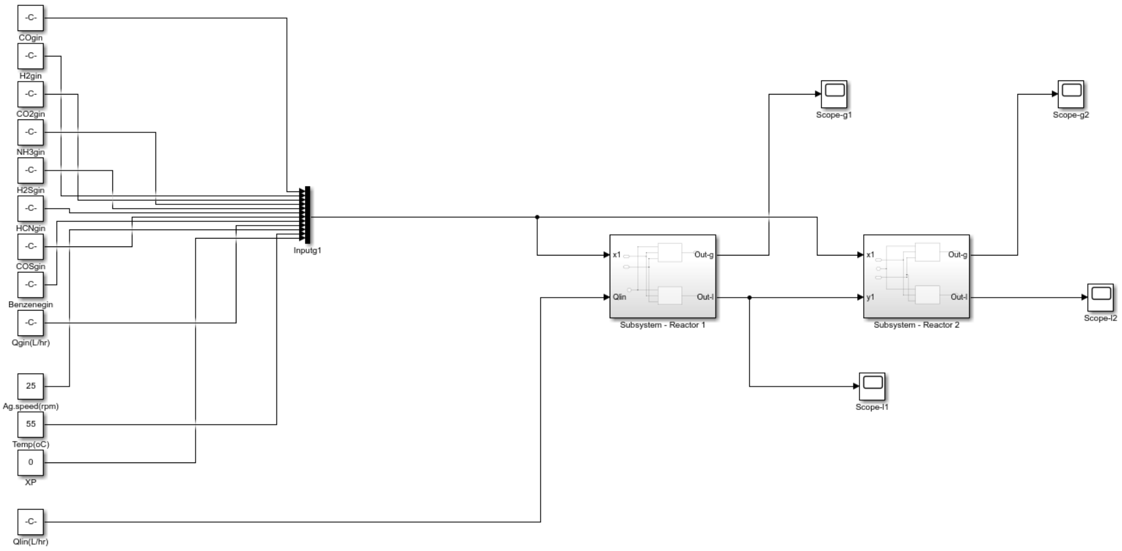

Figure 14: Syngas fermentation model in Simulink

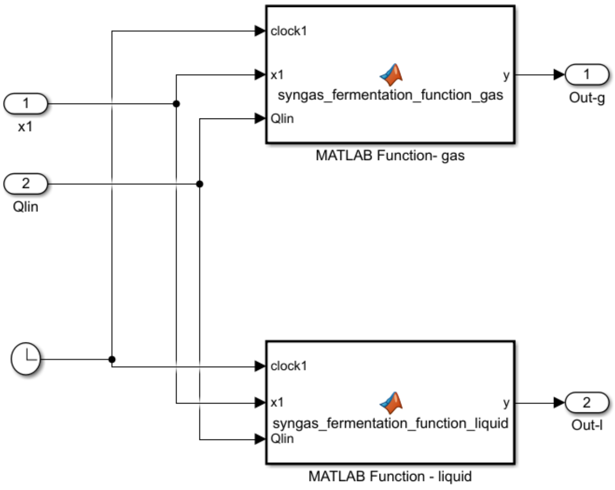

Figure 15: Subsystem depicting the reactor of syngas fermentation

The Simulink model, shown in Figure 14, comprises inputs including the syngas flow rate and composition, operating conditions that are agitation speed and temperature, and the medium flow rate. These inputs are connected to a subsystem representing the first reactor. The outputs from this subsystem are the gas and liquid concentrations exiting the reactor. The syngas fermentation process, as previously explained, consists of a total of 30 reactors, where the liquid medium enters each reactor in series, while syngas enters each reactor in parallel.

For the second reactor, the liquid inlet is the liquid output from the first reactor, and the syngas flow rate and composition remain the same as in the first reactor. Acetate is transferred from one reactor to the next until it exits from the final reactor. It is crucial to note that the final acetate concentration should not exceed 30 g/L to avoid accumulation.

In Figure 15, the reaction subsystem is depicted, which consists of two MATLAB functions. One function is for the gas phase and the other for the liquid phase. Each function solves the mass balances as previously described.

4.1.1.2 Validation of the dynamic simulation

The validation of the dynamic simulation of syngas fermentation involves comparing the concentration of the produced components with the results from D6.2 [2]. In the dynamic model, the produced acetate concentration from the first and the second reactor is the same, equal to 0.0164 mol/L. Therefore, it can be assumed that all the reactors will exhibit the same behavior, and the total concentration of the products is the concentration after the first reactor multiplied by the number of reactors, which is 30. The final acetate concentration after the 30th reactors equals to 29.5 g/L. The results from D6.2 [2] and from the dynamic simulation are summarized in Table 12 for comparison.

Table 12: Results from D6.2 and dynamic simulation

Final concentration (mol/L)	**Dynamic simulation**	**D6.2** [2]
Acetate	29.5	30

Table 12 indicates that the final acetate concentration from the dynamic simulation of syngas fermentation closely match that of D6.2 [2]. This validation confirms that the model accurately represents the behavior of the syngas fermentation process. Figure 16 illustrates the concentration profiles of CO, H_2, CO_2 and the produced acetate from the first reactor.

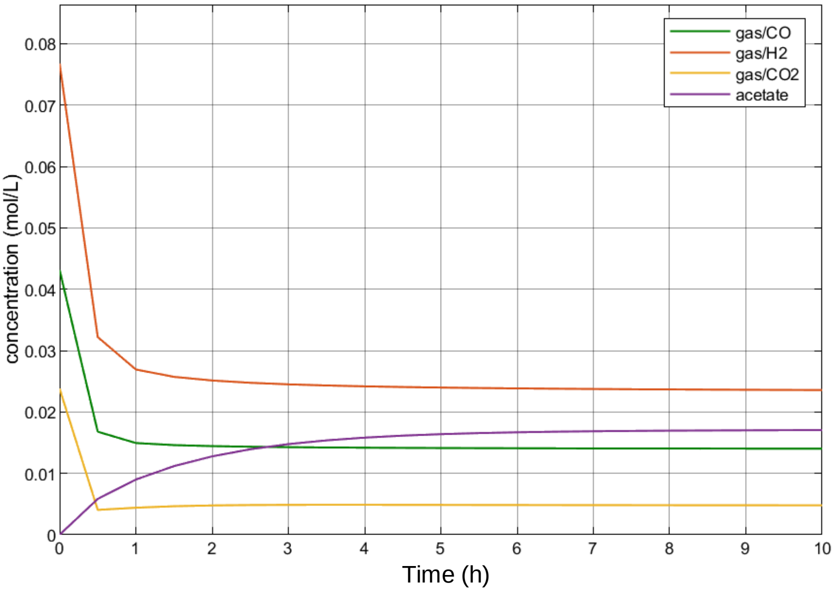

Figure 16: Concentration profiles of CO, H_2, CO_2 and acetate

Based on Figure 16, it can be observed that syngas is consumed in the first hour, while acetate is produced. The conversion rates $\left(equal\ to\ \frac{final-initial\ concentration}{initial\ concentration}\right)$ of CO, H_2 and CO_2 are then 67.5%, 70% and 69%, respectively.

4.1.2 Acetate fermentation

4.1.2.1 Model description and parameter fitting

Mass balance equations:

As for acetate fermentation, the dynamic model of the growth and lipid production phases is developed based on the mass balance equations of the process, assuming that the bioreactors operate continuously [20]. Hence, the liquid volume, V_l, variation is stable and equal to its initial value. In both stages, pH regulation is crucial and can be controlled at 7 by adding a pH regulatory solution. During continuous culture, pH is only controlled by KOH addition, considered negligible compared to the feed medium addition [20]. As for the feed medium flow rate, F, in both phases, it is set at 30623 L/h. In growth phase, it consists of acetate and ammonium as carbon and nitrogen sources with compositions of 30.5 g/L and 0.18 g/L, respectively. The C/N ratio (kg/kg) of this mixture is 45. In the lipid production phase, the composition of the feed is the one produced from the syngas fermentation, with 28.3 g/L acetate and 0.057 g/L NH_3. Hence, the C/N ratio at this stage is 130. The acetate fermentation operates in aerobic conditions, so air enters with flow rate at 764245 L/h.

The model can then be described by the cell mass concentration, X, changes in the reactor, as shown in Equation 58, and the concentration variation in the reactor for liquid solute or a dissolved gas compound i, Equation 59. The components, i, are the acetate, TAGs, NH_3, and O_2 and CO_2 in the liquid phase.

$$\frac{dX}{dt} = \frac{1}{V_l}(R_X - X \cdot V_l - F \cdot X) \qquad \text{Equation 58}$$

$$\frac{dS_i}{dt} = \frac{1}{V_l}\left(R_{Si} - S_i \cdot V_l + F\left(S_{ifeed} - S_i\right)\right) + k_l a(S_i^* - S_i) \qquad \text{Equation 59}$$

The mass balance of the O_2 and CO_2 in the gas phase, j, is described by Equation 60.

$$\frac{dC_{G,j}}{dt} = \left(\frac{1}{V_G}\right)\left(Q_{G,in} \cdot C_{G,j,in} - Q_{G,out} \cdot C_{G,j}\right) - k_L a_j \left(\frac{C_{G,j}}{m_{j,}} - C_{L,j}\right)\left(\frac{V_L}{V_G}\right) \qquad \text{Equation 60}$$

In the growth phase, the differential equation for TAGs production is set to 0, as TAGs are not produced during this phase. In the lipid production phase, the differential equation for cell mass concentration, X, equals to 0, as TAGs are produced within the cells, resulting in a constant amount. The equations above involve the mass transfer coefficient, $k_L a$, calculated as in syngas fermentation and the dissolved gas concentration in saturation conditions, S_i^*. The parameters m_j are the gas-liquid equilibrium factors, listed in Annexes along with the diffusion coefficients at infinite dilution in water, D_f.

Reaction rates:

The production rates of biomass, R_X, and the compounds involved in the reaction, R_{Si}, are calculated using algebraic equations [20]. The biomass production rate, R_X, is associated to the Monod kinetic law, as given by Equation 61, [20].

$$R_X = \mu_{max} \cdot \frac{S_{ac}}{Ks + S_{ac}} \cdot \frac{S_N}{K_{SN} + S_N} \cdot \frac{S_{O2}}{K_{SO2} + S_{O2}} \cdot X \qquad \text{Equation 61}$$

Where μ_{ma} represents the maximal growth rate, and K_s, K_{SN}, K_{SO2}, are the “half velocity” constants for the respective concentrations.

The production rate of the compounds involved in reactions, R_{Si} are calculated as in Equation 62, [20]:

$$R_{Si} = \frac{1}{Y_{X/i}} \cdot R_X \qquad \text{Equation 62}$$

With $Y_{X/i}$ the mass yield of each compound i calculated from the stoichiometric equations.

The lipid production rate, R_L, is expressed as shown iEquation 63, [20].

$$R_L = B \cdot X \cdot \frac{S_{ac}}{Ks+S_{ac}} \cdot \frac{S_N}{K_{SN}+S_N} \cdot Shift_{RL} \cdot lim_{lip} \qquad \text{Equation 63}$$

e B, is the lipid formation rate.

$ShiftRL$, is the metabolic shift toward lipid production calculated from Equation 64:

$$Shift_{RL} = 1 - \frac{1 + e^{-100\frac{1-I1}{I1}}}{1 + e^{-100\frac{limN-I1}{I1}}} \qquad \text{Equation 64}$$

Up to a certain lipid content, lipid production stopped and this is expressed by lim_{lip}, as Equation 65:

$$lim_{lip} = 1 - \frac{1 + e^{-100\frac{1-I2}{I2}}}{1 + e^{-100\frac{\%lip-I2}{I2}}} \qquad \text{Equation 65}$$

Where $\%lip = \frac{S_{lip}}{DCW}$, with DCW being the total dry cell weight.

The maintenance is described by the acetic acid oxidation without cell mass or storage compounds synthesis, described by R 21, [20]:

$$Acetate + 2\ O_2 \rightarrow 2\ CO_2 + H_2O \qquad \text{R 21}$$

The associated kinetic law could be written as in Equation 66, [20]:

$$R_m = mX \frac{S_{ac}}{Ks + S_{ac}} \frac{S_{O2}}{K_{SO2} + S_{O2}} \left(1 - \frac{R_X}{\mu_{max} X}\right)\left(1 - \frac{R_L}{BX}\right) \qquad \text{Equation 66}$$

Where m is the maintenance term.

The R_{Si} equation of each compound is finally illustrated in Table 13:

Table 13: Production rate equations of the compounds involved in reactions

Component	R_{Si}
Acetate	$R_{ac} = -\left(\frac{1}{Y_{xac}}\right) R_x - R_m - \left(\frac{1}{Y_{lac}}\right) R_L$
O₂	$R_{O2} = -\left(\frac{1}{Y_{xO2}}\right) R_x - \frac{1}{2} R_m$
CO₂	$R_{CO2} = \left(\frac{1}{Y_{xCO2}}\right) R_x + 2R_m$
NH₃	$R_{NH3} = \left(\frac{1}{Y_{xNH3}}\right) R_x$

Estimation of model parameters:

The unknown parameters expressed above, that are the $\mu_{max}, K_s, K_{SN}, K_{SO2}, B, I_1, I_2, Y_{Xac}, Y_{XO2}, Y_{XN}, m, f_0, Y_{lac}, Y_{xCO2}$ and Agitation Speed are estimated using the maximum likelihood principle (MLP), [18], with data retrieved from experimental data from D3.5 [17] and then from industrial-scale data from D6.2 [2], that are these being used in the dynamic simulation. The fitted parameters and the dynamic profile of each case are illustrated in Annexes, assuming that the acetate fermentation operates at 28 ºC and 1 bar. Given the high nonlinearity of the MLP method, the objective function is minimized using the "fmincon" function in MATLAB. This approach ensures a good initial estimation of parameters, enhancing the accuracy of the MLP results.

Model simulation:

After the kinetic parameters are fitted to the industrial-scale data, the acetate fermentation process is simulated in Simulink and its results are compared against those from D6.2 [2] to validate the model. The dynamic model of acetate fermentation is a nonlinear algebraic-differential system, demanding numerical solvers suitable for stiff problems. Therefore, as syngas fermentation, the ode15s method from MATLAB is used for time integration setting as feedstock the final concentration of syngas fermentation. The Simulink models depicting the growth reactor are illustrated in Figure 17, and three of the 29 reactors for the lipid production phase are shown in Figure 18 and Figure 19. These figures provide a visual representation of the setup and operation of the fermentation process within the reactors.

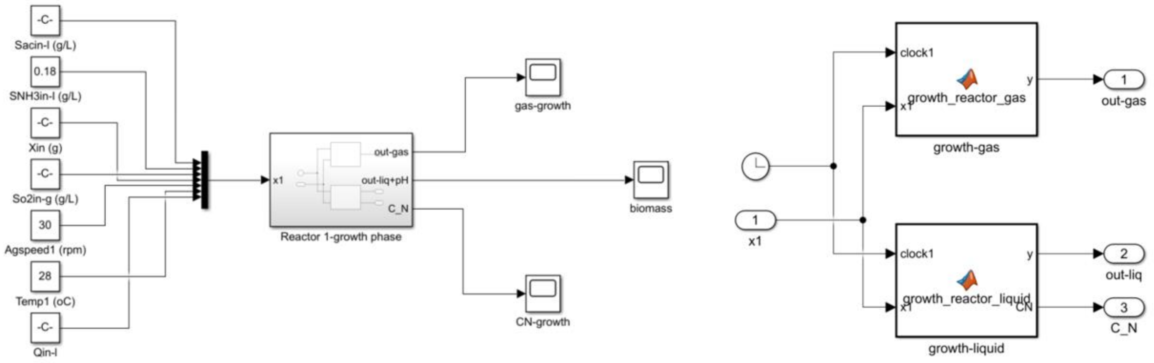

Figure 17: Growth production phase model in Simulink and subsystem of the reactor

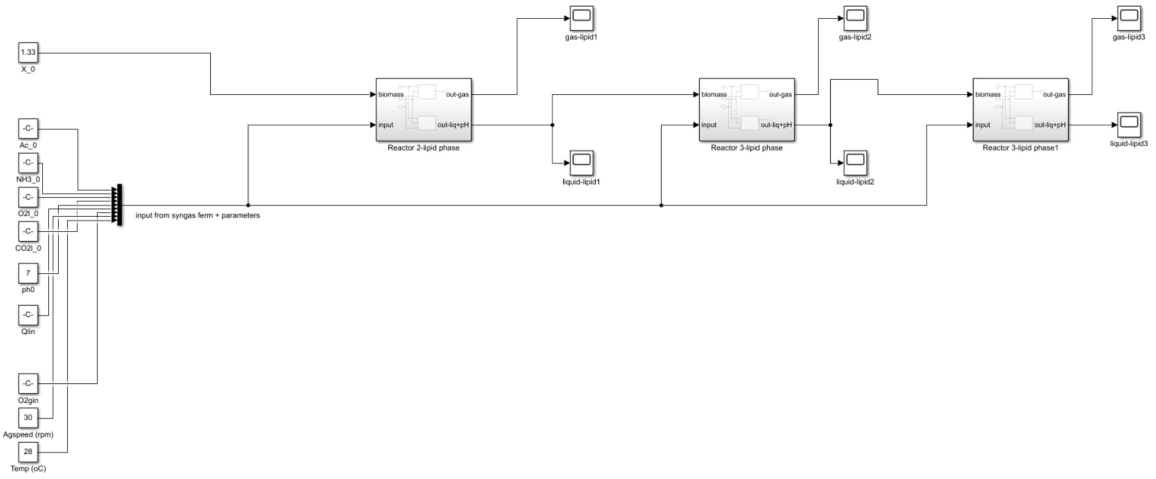

Figure 18: Lipid production phase model in Simulink

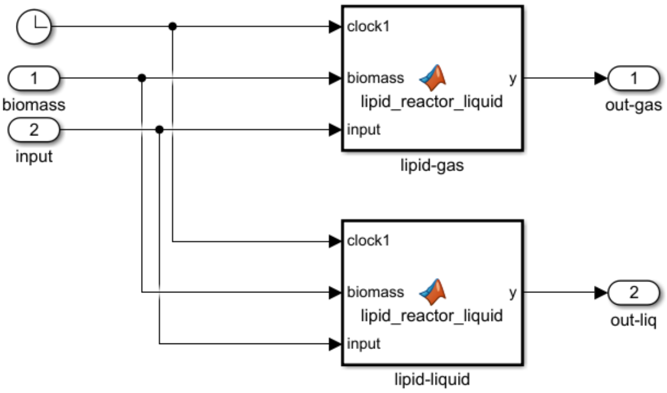

Figure 19: Subsystem depicting the reactor for lipid production

In the growth phase, Figure 17, the main input values are the medium and air, with the biomass concentration exiting the reactor. This biomass, along with the medium flow rate and composition, operating conditions such as agitation speed and temperature, and the oxygen concentration and flow rate are the inputs for the lipid production phase, Figure 18. These inputs are connected to a subsystem representing the first reactor. The outputs from this subsystem are the gas and liquid concentrations exiting the reactor. The acetate fermentation process, as previously explained, consists of 30 reactors: one for the growth phase and the others for lipid production. In the lipid production reactors, the biomass enters each reactor in series, while acetate produced in syngas fermentation and air enter each reactor in parallel. Figure 19 depicts the reaction subsystem, which consists of two MATLAB functions. One function is for the gas phase and the other for the liquid phase. Each function solves the mass balances as previously described.

4.1.2.2 Validation of the dynamic simulation

The validation of the dynamic simulation of acetate fermentation involves a comparison of the concentration of the produced components with the results from D6.2 [2]. During the growth phase, an increase in the C/N ratio is expected as the biomass is cultured. According to the dynamic model, the final C/N ratio after biomass production is expected to reach 230.

Figure 20 illustrates the concentration profiles of biomass, acetate, TAGs and NH_3 as well as the C/N ratio profile of the growth phase.

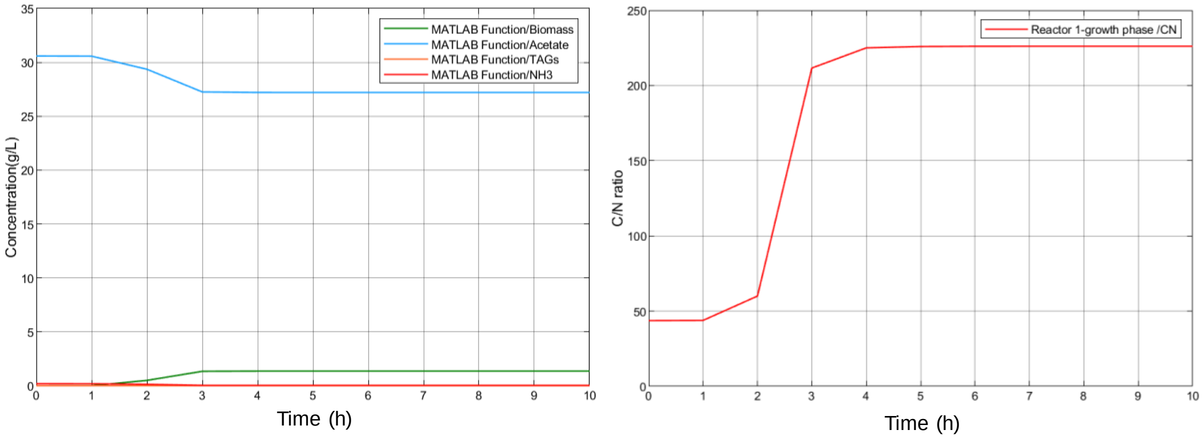

Figure 20: Concentration profiles of components and C/N ratio in the growth phase

Analysis of Figure 20 reveals that during the growth phase, acetate and NH_3 are consumed, resulting in the production of biomass. Hence, as expected, the C/N ratio increases. It is noteworthy that TAGs are not produced during this growth phase.

As for the liquid production phase, based on the dynamic model, the produced lipid concentration from the first and the second reactor is the same, equal to 0.24 g/L. Therefore, it can be assumed that all the reactors will exhibit the same behavior, and the total concentration of the products is the concentration after the first reactor multiplied by the number of reactors, which is 29. So, a final TAGs concentration after the 29th reactor of 6.96 g/L is achieved. The results from D6.2 [2] and from the dynamic simulation are summarized in Table 14 for comparison.

Table 14: Results from D6.2 and dynamic simulation

Components	Dynamic simulation	D6.2
TAGs (g/L)	7.0	7.3
Acetate (g/L)	0.061	0

Table 14 indicates that the final concentrations from the dynamic simulation of acetate fermentation closely match those from D6.2 [2]. This validation confirms that the model accurately represents the behavior of the acetate fermentation process.

Figure 21 illustrates the concentration profiles of biomass, acetate, TAGs and NH_3 of the first reactor of lipid production phase. It is observed that acetate is consumed in the first hour, while TAGs are produced in the biomass cells, which remain constant.

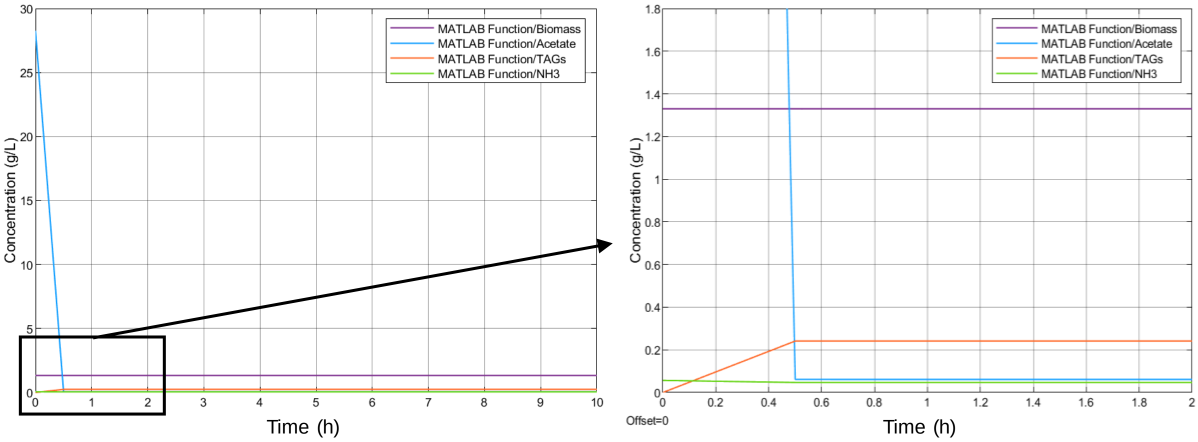

Figure 21: Concentration profiles of components for lipid production phase

4.2 Control system

To develop a plant-wide control design system, it is crucial to carefully select the controlled variables. The plant-wide control design refers to the structure of the controller rather than the control algorithm or control law itself. It is crucial to ensure that each controlled variable is sensitive to its corresponding manipulated variable.

In the syngas fermentation process, the controlled variable is the acetate concentration which can be manipulated by adjusting the agitation speed. In acetate fermentation, the lipid and acetate concentrations are controlled by adjusting the biomass concentration via operational parameters of the growth phase such as agitation speed, C/N ratio and oxygen flowrate. The control system for the growth phase is not executed in this deliverable.

For each fermentation process, a PID controller with closed-loop feedback control is created and tuned. In industrial applications, PID controller tuning is often done empirically [21]. The model is then utilized to analyze the impacts of varying syngas composition (molar concentrations of CO, H_2 and CO_2) in syngas fermentation and liquid flow rate and acetate concentration in acetate fermentation, on the manipulated variable.

Following, in paragraphs 4.2.1 and 4.2.2, the control system for the two fermentation processes is described in detail.

4.2.1 Syngas Fermentation

4.2.1.1 Description and validation

To develop the control system for the syngas fermentation process, it must be proved that the controlled variable, acetate concentration, is influenced by the manipulated variable, agitation speed. To accomplish this, several agitation speeds are set in the model, and the acetate concentration from first reactor is retrieved. Figure 22 depicts the sensitivity of acetate concentration with time to agitation speed.

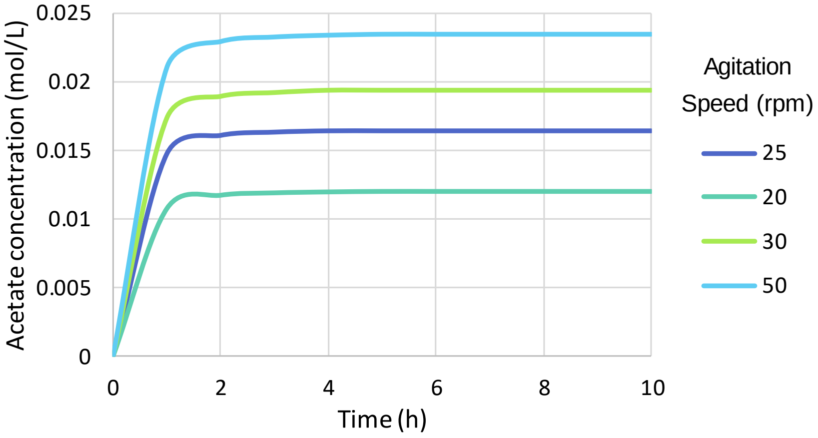

Figure 22: Diagram of acetate concentration profile for different agitation speeds

Subsequently, the control system is developed by incorporating a PID (Proportional-Integral-Derivative) controller with feedback control into the Simulink model, as illustrated in Figure 23.

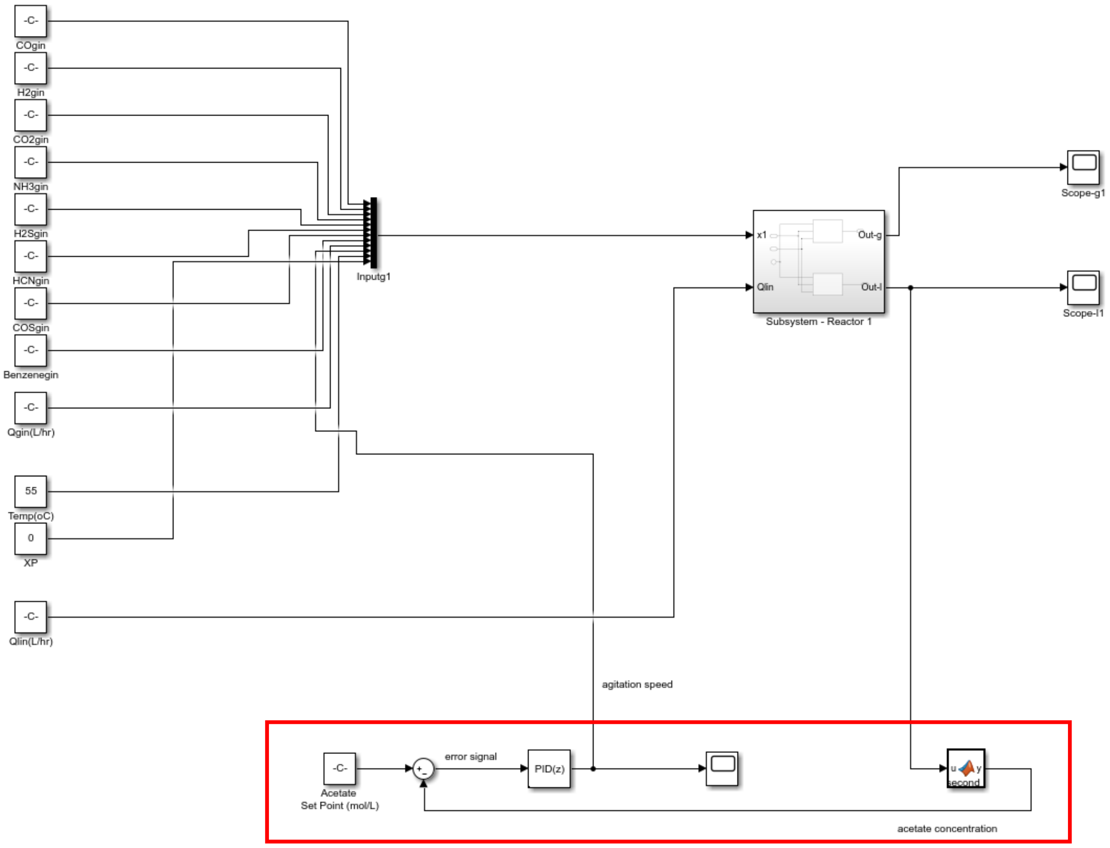

Figure 23: Control system for syngas fermentation

The PID controller operates by calculating an error signal, which is the difference between the desired set point of acetate concentration (0.0164 mol/L) and the actual output of the system. This error signal is then used to adjust the agitation speed to the system in order to minimize the error and keep the system operating at the desired set point. The PID controller operates in discrete time, which means that the control signal is updated only at these discrete points in time.

To tune the PID parameters (K_p, T_I, T_d), a trial-and-error method is used in each case until the controller achieves a steady state. To validate the PID controller for the base case previously described, the agitation speed is adjusted to 25 rpm to achieve the desired acetate concentration, as illustrated in Figure 24.

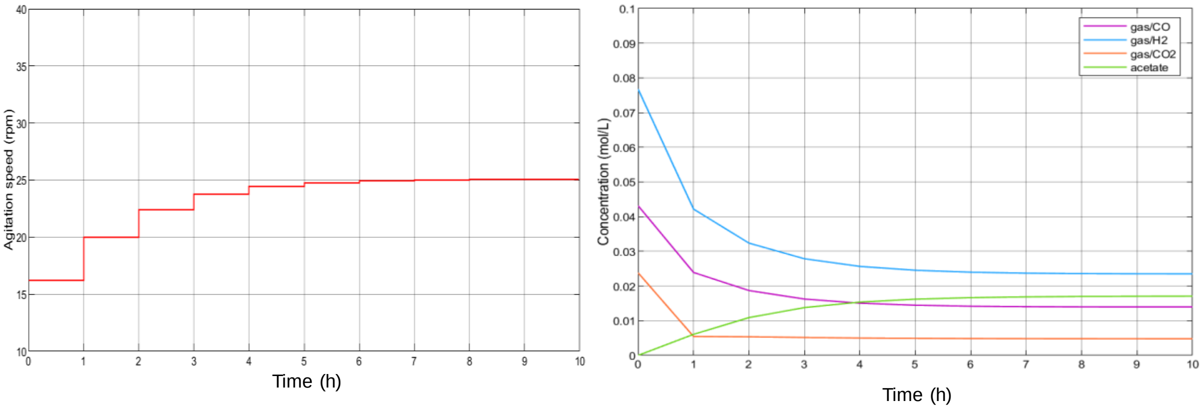

Figure 24: Diagram of agitation speed and concentration of components to time

Figure 24 shows that after 5 hours, the acetate concentration is fixed to the set point, as the agitation speed remains constant at 25 rpm. Therefore, the control system is deemed valid.

4.2.1.2 Results for different cases

The model is then utilized to analyze the impacts of varying syngas composition (molar concentrations of CO, H_2 and CO_2) on the agitation speed. The studied cases are described in Table 15.

Table 15: Different cases of syngas composition

	Syngas molar concentration		
Cases	CO	H_2	CO_2
A	0.0431	0.0768	0.0238
B	**0.0647**	0.0768	0.0238
C	**0.0216**	0.0768	0.0238
D	0.0431	**0.1152**	0.0238
E	0.0431	**0.0461**	0.0238
F	0.0431	0.0768	**0.0357**
G	**0.0647**	**0.1152**	**0.0357**

Analyzing Table 15, case A represents the initial syngas composition. In cases B and C, the CO molar concentration increases and decreases by 50%, respectively, while the H_2 and CO_2 molar concentrations remain constants. In cases D and E, H_2 molar concentration increases and decreases by 50% and 40%, while the CO and CO_2 molar concentrations remain constants. In F case, CO_2 molar concentration increase by 50%. Finally, in case H, all molar concentrations increase by 50%.

By inserting each variation through a step input in the controlled model, the agitation speed is adjusted to maintain the acetate concentration at the desired point of 0.0164 mol/L, after the first reactor. The results of the agitation speeds for all cases and the K_p, T_I, T_D coefficients of each PID controller are shown in Table 16.

Table 16: PID coefficients and adjusted agitation speed in different cases

Case	PID controller			Controlled acetate concentration (mol/L)	Adjusted agitation speed (rpm)
	K_P	T_I	T_D		
A	70	250	0	0.0164	25
B	150	400	0	0.0162	23
C	70	150	0	0.0161	27
D	70	300	0	0.0161	20
E	70	450	0	0.0160	73
F	70	350	0	0.0163	25
G	70	200	0	0.0166	19

From Table 16, it can be observed that varying the CO and H_2 molar concentrations (Cases B-E) results in changes in agitation speed, indicating that CO and H_2 have an influence on the final concentration of acetate. Conversely, CO_2 (Case F) does not significantly impact the final acetate concentration, as the agitation speed of the controlled system remains constant. Upon analyzing the results of agitation speed from the PID controller for cases B and C, it is noted that agitation speed exhibits a small change in response to CO variations. However, when varying the H_2 molar concentration (cases D and E), the agitation speed changes considerably, highlighting its importance.

The dynamic responses of reactants and acetate, as well as the responses of the PID controller for cases B and D, are illustrated in Figure 25 and Figure 26, respectively.

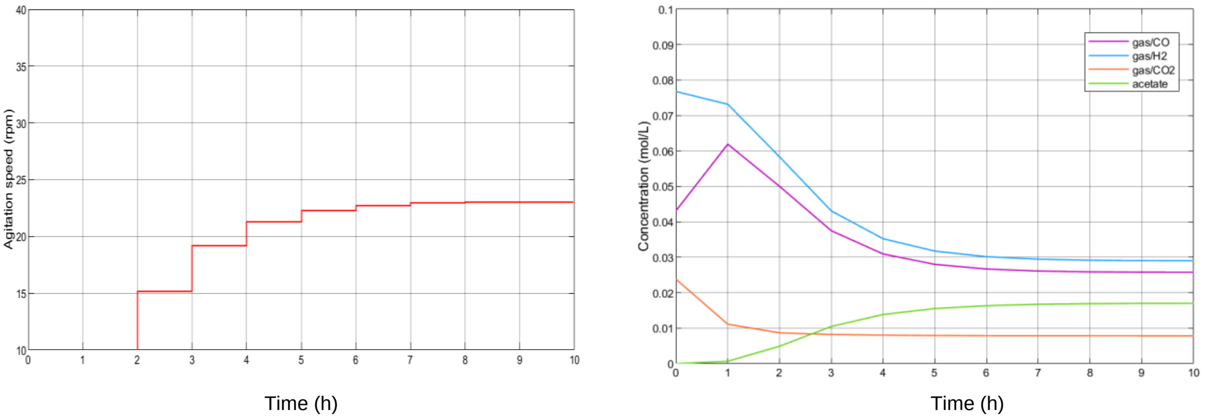

Figure 25: Diagram of agitation speed and concentration of components to time for controlled system of case B

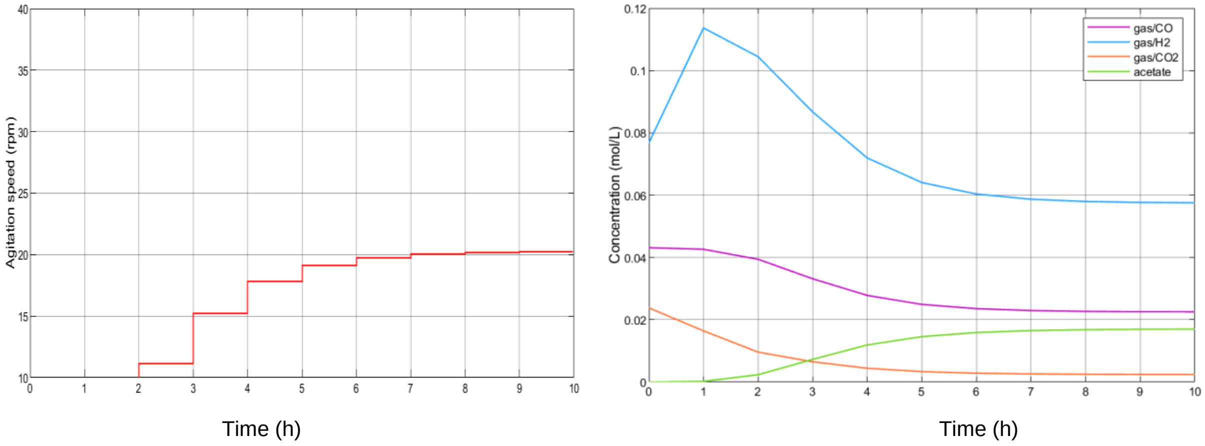

Figure 26: Diagram of agitation speed and concentration of components to time for controlled system of case D

Figure 25 and Figure 26 illustrate the dynamic responses of the concentrations of the components by varying the syngas composition in the first hour. Additionally, the figures display the agitation speed at every discrete time for 10 hours. In both cases, the controller reaches the set point after 7 hours.

As previously mentioned, cases D and E are the two with the more obvious variation. After implementing the PID controller in the dynamic simulation, the comparison between the dynamic response of the system without the agitation speed adjustment (uncontrolled) and the controlled system is illustrated in Figure 27 and Figure 28 for cases D and E, respectively.

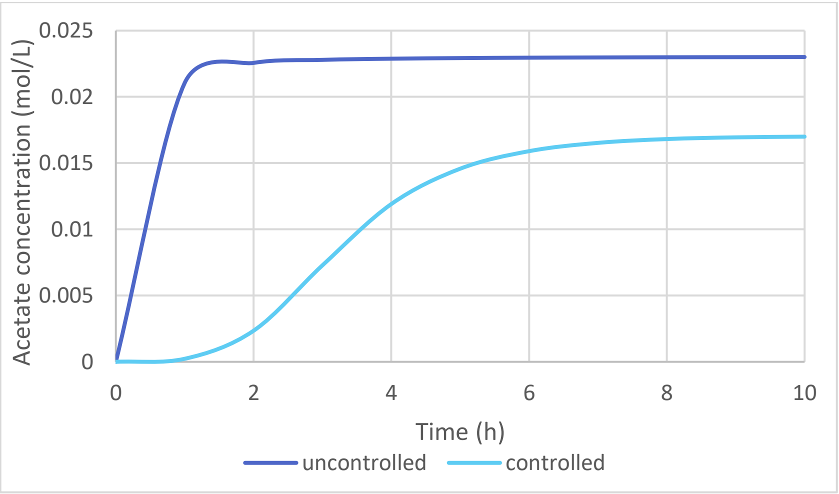

Figure 27: Dynamic response of acetate concentration for case D, comparing the controlled and uncontrolled system

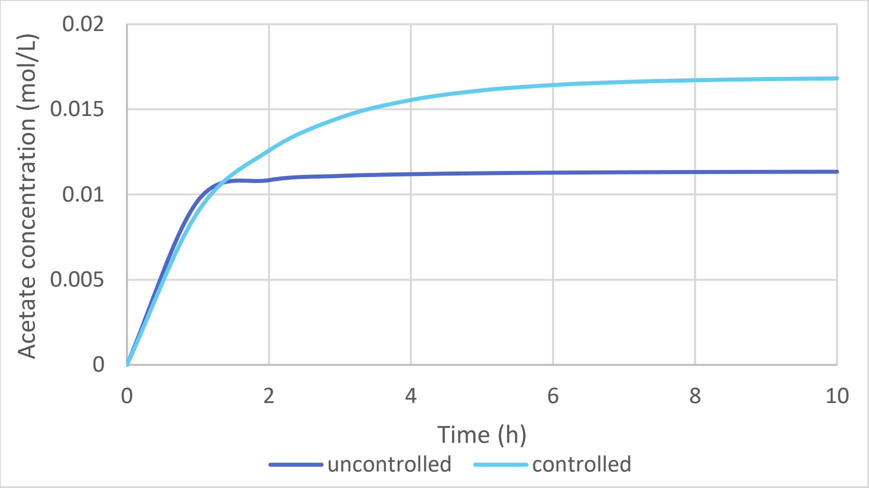

Figure 28: Dynamic response of acetate concentration for case E, comparing the controlled and uncontrolled system

These visualizations further emphasize the significant impact of varying the H_2 molar concentration on the acetate concentration and highlight the importance of the control system in maintaining the desired acetate concentration by adjusting the agitation speed to avoid accumulation. The delay of the controlled system in achieving a steady state condition is due to the controller and it could be decreased by changing its coefficients.

4.2.2 Acetate fermentation

4.2.2.1 Description and validation

As it was previously described, the control system is developed to adjust the biomass concentration -through manipulating the operational parameters of biomass growth phase- due to variations in liquid flow rate or acetate concentration. To develop the control system for the lipid production phase of acetate fermentation process, it must be proved that the controlled variable, the final acetate concentration, is influenced by the manipulated variable, biomass concentration. To accomplish this, several initial biomass concentrations are set in the model, and the final acetate concentration from first reactor is retrieved. The different studied cases are the biomass concentration for the fitted model (Case 1), 30% over Case 1 (Case 2), and 30% less than Case 1 (Case 3). Table 17 depicts the sensitivity of acetate concentration when varying the biomass concentration.

Table 17: Results of final acetate concentration for different biomass concentrations

Case	Biomass concentration (g/L)	Final acetate concentration (g/L)
1	1.33	0.061
2	0.93	0.087
3	1.7	0.047

These results show the final acetate concentrations achieved for the different cases. It is also noteworthy that in all cases, the TAGs concentration remains constant at 0.24 g/L. Subsequently, the control system is developed by incorporating a PID (Proportional-Integral-Derivative) controller with feedback control into the Simulink model, as illustrated in Figure 29.

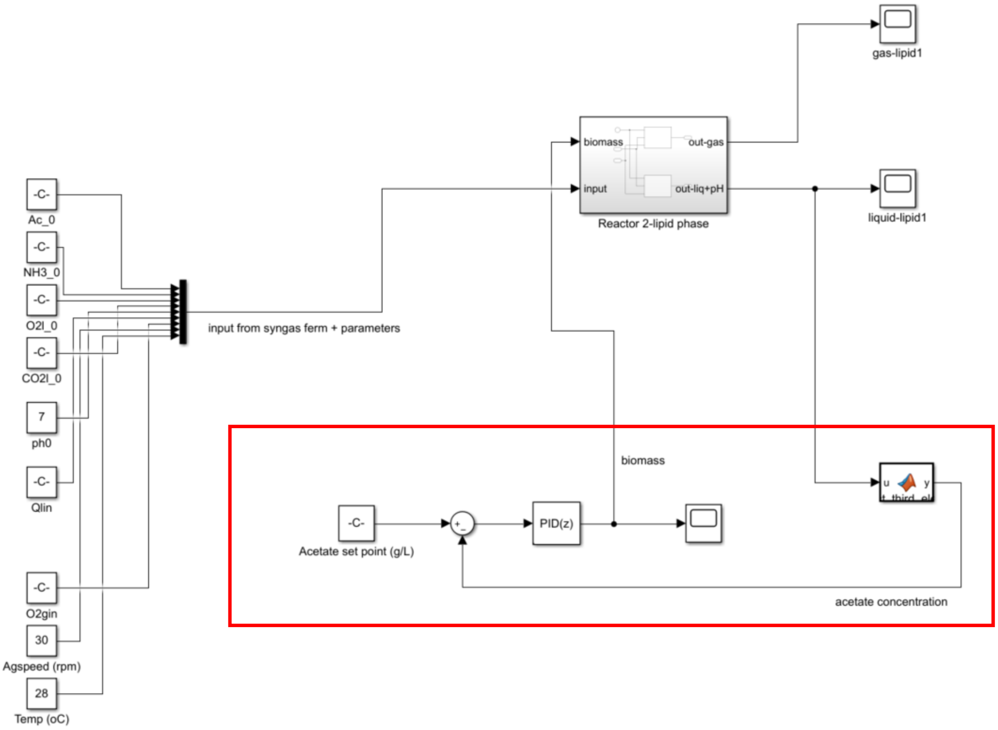

Figure 29: Control system for lipid production phase of lipid fermentation

The PID controller operates by calculating an error signal, which is the difference between the desired set point of acetate concentration at 0.06 g/L and the actual output of the system. This error signal is then used to adjust biomass concentration via biomass growth operational parameters to the system in order to minimize the error and keep the system operating at the desired set point. The PID controller operates in discrete time, which means that the control signal is updated only at these discrete points in time.

To tune the PID parameters (K_p, K_I, K_d), a trial-and-error method is used until the controller achieves a steady state. To validate the PID controller for the base case previously described, the biomass concentration is adjusted to 1.4 g/L to achieve the desired acetate concentration, as illustrated in Figure 30.

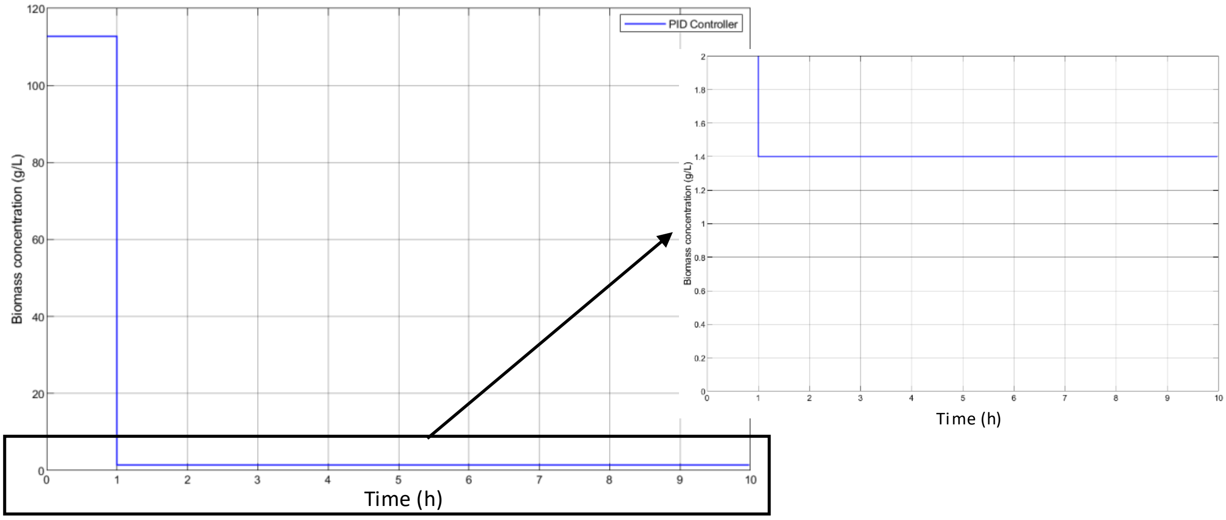

Figure 30: Diagram of biomass concentration to time

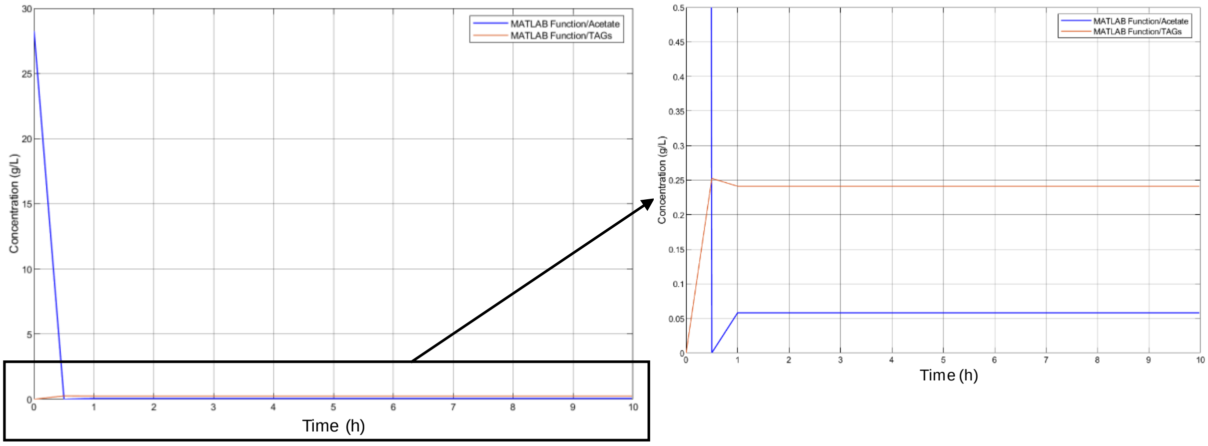

Figure 31: Diagram of final acetate and TAGs concentration to time

Figure 30 and Figure 31 show that after an hour, the final acetate concentration is fixed to the set point, as the biomass concentration remains constant at 1.4 g/L. Therefore, the control system is deemed valid.

4.2.2.2 Results for different cases

The model is then utilized to analyze the impacts of varying liquid flow rates and acetate concentration on the final acetate concentration. The second variation would occur in case of difficulty in controlling syngas fermentation. The studied cases are described in Table 18.

Analyzing Table 18, Case A represents the initial liquid flow rate and acetate concentration. In cases B and C, the liquid flow rate decreases and increases by 20%, respectively. In cases D and E, the acetate concentration decreases and increases by 20%, respectively.

Table 18: Different cases of liquid flow rate

Case	Liquid flow rate, $Q_{l,in}$	Acetate concentration (g/L)
A	30623	28.3
B	**24498**	28.3
C	**36747**	28.3
D	30623	**22.6**
E	30623	**33.9**

By inserting each variation through a step input in the controlled model, the biomass concentration is adjusted to maintain the final acetate concentration at the desired point of 0.06 g/L, after the first reactor. The results of the biomass concentration for all cases and the K_p, T_I, T_D coefficients of each PID controller are shown in Table 19.

Table 19: Adjusted biomass concentration in different cases

Case	PID controller			Controlled final acetate concentration (g/L)	Adjusted biomass concentration (g/L)
	K_P	T_I	T_D		
A	-4	-0.05	0	0.058	1.4
B	-4	-0.04	0	0.058	1.12
C	-4	-0.06	0	0.060	1.64
D	-4	-0.04	0	0.056	1.11
E	-4	-0.06	0	0.061	1.67

Based on the data presented in Table 19, it is evident that an increase in the liquid flow rate or in acetate concentration corresponds to a higher biomass concentration. Conversely, a decrease in the liquid flow rate is associated with a lower biomass concentration.

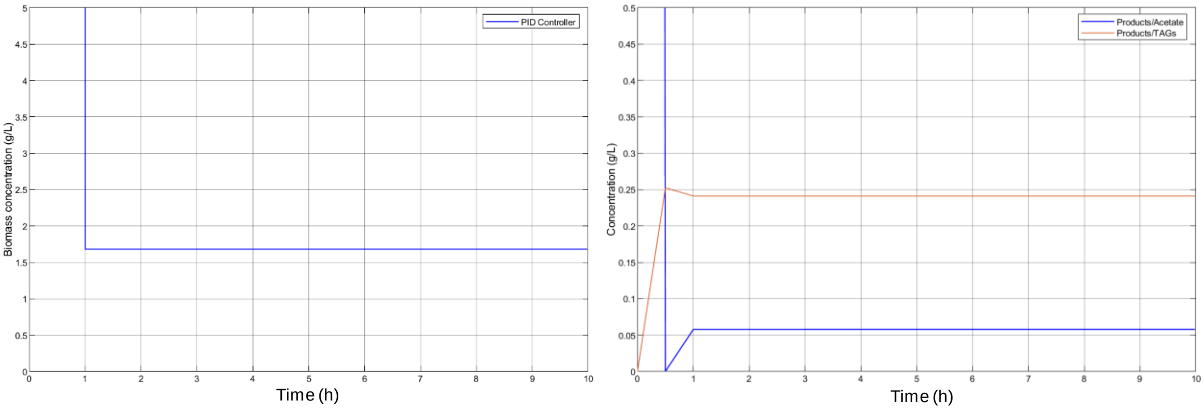

Figure 32: Diagram of biomass concentration and TAGs and acetate concentration to time for controlled system of case C

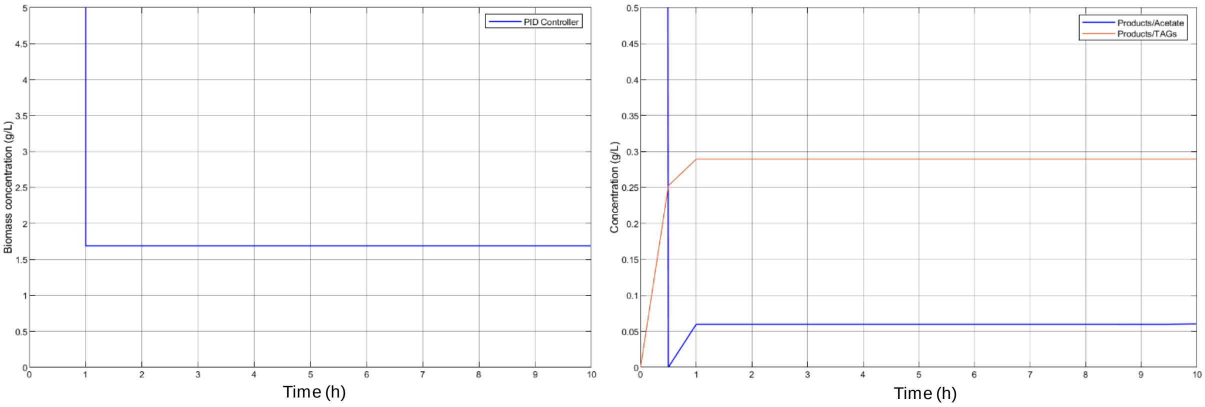

Figure 33: Diagram of biomass concentration and TAGs and acetate concentration to time for controlled system of case E

Figure 32 and Figure 33 illustrate the dynamic response of the acetate and TAGs concentrations by varying the liquid flow rate or the acetate concentration in the first hour. Additionally, the figure displays the biomass at every discrete time for 10 hours. In both cases, the PID controllers achieve the desired set point in an hour.

After implementing the PID controller in the dynamic simulation, the comparison between the dynamic response of the system without the biomass adjustment (uncontrolled) and the controlled system is illustrated in Figure 34 and Figure 35 for cases C and E, respectively.

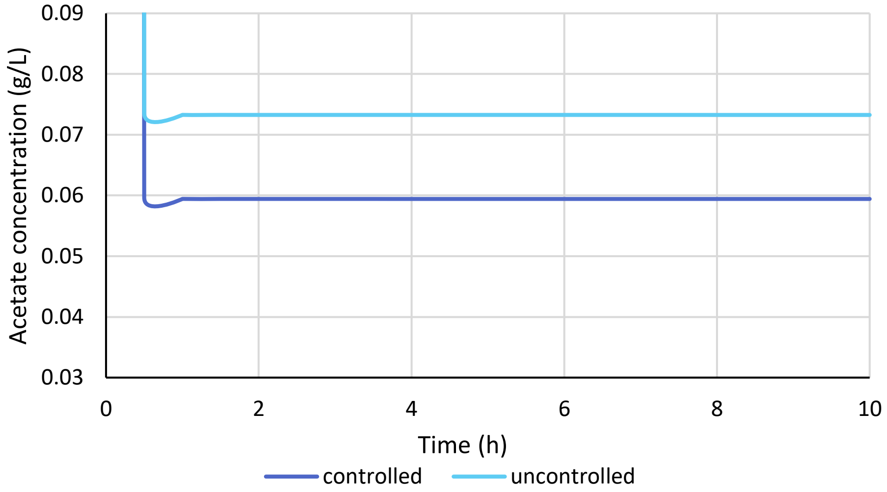

Figure 34: Dynamic response of acetate concentration for case C, comparing the controlled and uncontrolled system

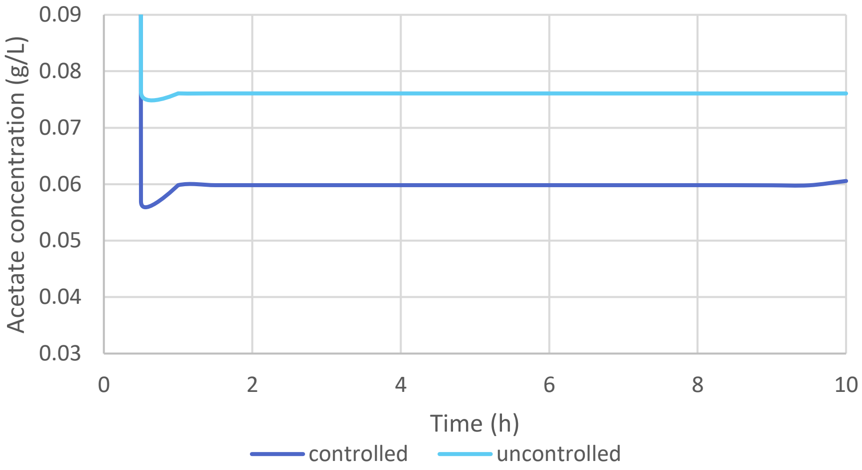

Figure 35: Dynamic response of acetate concentration for case E, comparing the controlled and uncontrolled system

These visualizations further emphasize the significant impact of different liquid flow rates or acetate concentrations on the biomass concentrations and highlight the importance of the control system in maintaining the desired final acetate concentration.

5 Thermocatalytic part

5.1 Steady state model and export to Aspen Dynamics

An new Aspen model had to be developed because the model that was built and used for the simulation runs in Task 2.5 and Task 6.2 could not be exported to Aspen Dynamics and be the basis for the dynamic simulation analysis.

5.1.1 Model description

Figure 36 shows the Aspen model for the thermocatalytic part. As in the respective pilot unit at Task 5.4, the hydroprocessing is carried out in two reactors. In the first one, the conversion reactions of triglycerides into paraffins take place whereas in the second reactor, the isomerization and hydrocracking reactions occur. Since no CO or CO_2 were detected in gas analysis at the pilot campaign (D5.4 [22] see Table 25) the decarboxylation and decarbonylation reactions are discarded assuming that they do not take place in the reactor.

Table 20. Initial reactions at 1st reactor

Reaction	Fractional conversion	No
$C_{51}H_{98}O_6 + 3H_2 \rightarrow 3C_{16}H_{32}O_2 + C_3H_8$	1	R 22
$C_{57}H_{104}O_6 + 3H_2 \rightarrow 3C_{18}H_{34}O_2 + C_3H_8$	1	R 23
$C_{57}H_{98}O_6 + 3H_2 \rightarrow 3C_{18}H_{32}O_2 + C_3H_8$	1	R 24
$C_{57}H_{110}O_6 + 3H_2 \rightarrow 3C_{18}H_{36}O_2 + C_3H_8$	1	R 25
$C_{18}H_{32}O_2 + H_2 \rightarrow C_{18}H_{34}O_2$	0.4	R 26
$C_{18}H_{32}O_2 + 2H_2 \rightarrow C_{18}H_{36}O_2$	0.6	R 27

The modeling of the first reactor is split into two parts. In the first one (HDR-01), the initial reactions of triglycerides decomposition (depropanation) are considered assuming total conversion into their respective free fatty acids, using a stoichiometric reactor (RSTOIC). Moreover, the linoleic acid ($C_{18}H_{32}O_2$) is converted into oleic ($C_{18}H_{34}O_2$) and stearic acid ($C_{18}H_{36}O_2$) through hydrogenation reaction (see Table 20, R 22 - R 27). In the second part (HDR-02), the hydrodeoxygenation (HDO) reactions of the fatty acids are considered. This reactor is modelled as a plug flow reactor (RPLUG). The kinetic models for stearic acid (R 28-R 30), oleic acid (R 31, R 32) and palmitic acid (R 33) HDO reactions were obtained from [23], [24] and [25] respectively but the kinetic constants were fine-tuned where needed in order the product yields to reach an agreement with the respective experimental data.

Table 21. HDO reactions kinetics parameters

Reaction	k	E (kJ/kmol)	Reaction expression[1]	No
$C_{18}H_{36}O_2 + H_2 \rightarrow C_{18}H_{36}O + H_2O$	5.52E-02	22700	$r_{HDO1} = \frac{ke^{\left(-\frac{E}{RT}\right)}C_{H_2}}{1+51.4C_{stearic}}\left[\frac{kmol}{kg_{cat}ms}\right]$	R 28
$C_{18}H_{36}O + H_2 \rightarrow C_{18}H_{37}OH$	2.78E-01	159000	$r_{HDO2} = \frac{ke^{\left(-\frac{E}{RT}\right)}C_{C18H36O}C_{H_2}}{1+51.4C_{stearic}}\left[\frac{kmol}{kg_{cat}ms}\right]$	R 29
$C_{18}H_{37}OH + H_2 \rightarrow C_{18}H_{38} + H_2O$	2.70E-02	117000	$r_{HDO3} = \frac{ke^{\left(-\frac{E}{RT}\right)}C_{C18H37OH}C_{H_2}}{1+51.4C_{stearic}}\left[\frac{kmol}{kg_{cat}ms}\right]$	R 30
$C_{18}H_{34}O_2 + H_2 \rightarrow C_{18}H_{34}O + H_2O$	195	57882	$r_{HDO4} = ke^{\left(-\frac{E}{RT}\right)}C_{oleic}\left[\frac{kmol}{kg_{cat}m^2s}\right]$	R 31
$C_{18}H_{34}O + 2H_2 \rightarrow C_{18}H_{36} + H_2O$	60	60341	$r_{HDO5} = ke^{\left(-\frac{E}{RT}\right)}C_{C18H34O}\left[\frac{kmol}{kg_{cat}m^2s}\right]$	R 32
$C_{16}H_{32}O_2 + 3H_2 \rightarrow C_{16}H_{34} + 2H_2O$	11.97E-05	60300	$r_{HDO5} = \frac{ke^{\left(-\frac{E}{RT}\right)}C_{palmitic}p_{H_2}}{1+2\cdot 10^{-6}e^{\left(-\frac{3180}{RT}\right)}p_{H_2}}\left[\frac{kmol}{kg_{cat}ms}\right]$	R 33

[1] Molar concentrations are expressed in kmol/m^3 and partial pressures in kPa

For the hydrocracker reactor modeling (HCR) a stoichiometric reactor is considered as there are no available kinetic data from the lab/pilot experiments or from the literature. The fractional conversion of each reaction was fine-tuned accordingly in order the product yields to reach an agreement with the respective measured fuels yields (see Table 22). Moreover, as there was no relevant information about the produced isomers and their yields, no isomerization reaction is considered.

Table 22. Hydrocracking reactions parameters (reactions occur in series)

reaction	Fractional conversion of hydrocarbon	No
C16H34 + H_2 → C_3H_8+ $C_{13}H_{28}$	0.371	R 34
C16H34 + H_2 → 2 C_8H_{18}	0.01	R 35
C17H36 + H_2 → C_3H_8+ $C_{14}H_{30}$	0.504	R 36
C17H36 + H_2 → C_9H_{20}+ C_8H_{18}	0.01	R 37
C17H36 + H_2 → $C_{10}H_{22}$ + C_7H_{16}	0.02	R 38
C18H38 + H_2 → C_3H_8+ $C_{15}H_{32}$	0.049	R 39
C18H38 + H_2 → C_7H_{16} + $C_{11}H_{24}$	0.45	R 40
C18H38 + H_2 → C_8H_{18} + $C_{10}H_{22}$	0.45	R 41
C18H38 + H_2 → 2 C_9H_{20}	0.01	R 42
C18H36 + 2 H_2 → $C_{15}H_{32}$ + C_3H_8	0.6	R 43
C18H38 + H_2 → $C_{14}H_{30}$ + n-C_4H_{10}	0.1	R 44

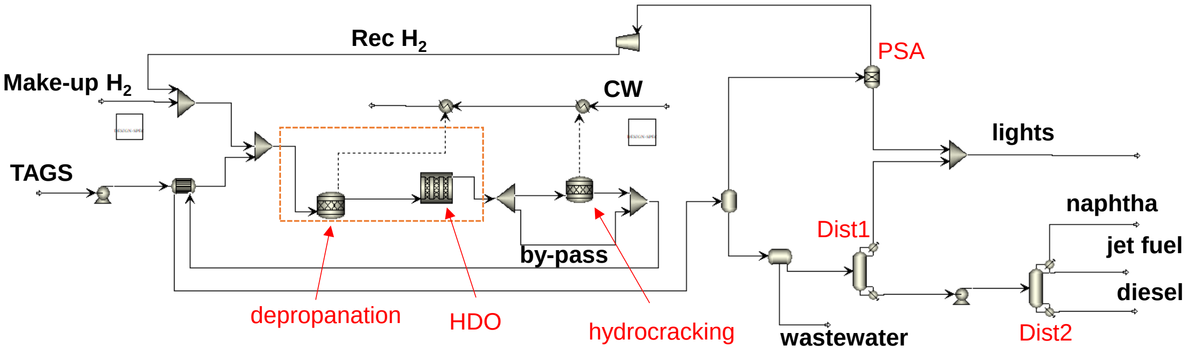

Figure 36. Aspen Plus flowsheet for TAGs hydroprocessing and refining

The fuels products separation and refining unit was inspired by [26] considering two distillation columns. Before them, the water is separated from the bio-crude in a decanter. At the first column, the light gas mainly consisting in propane is retrieved from the top. The naphtha, jet fuel and diesel fractions are separated in the second column. The lighter fractions naphtha and kerosene are obtained as gaseous and liquid distillates at the condenser, respectively, setting a condenser temperature of 180°C.

The Peng-Robinson property method was selected for the hydroprocessing reactor part, the gas recycling and gas/liquid products separation, while the Non-random two-liquid model for liquid activity coefficients calculations combined with Redlich-Kwong Soave Equation of state with Henry's law (NRTL-RK) was used for the refining part at the two distillation columns. Especially for the first column, the convergence option of Petroleum/Wide-boiling was selected as it was observed that better results were achieved.

Table 23. TAGs stream specifications

parameter	value
Mass flow rate (kg/s)	1.788
Temperature (°C)	25
Pressure (bar)	1
Tripalmitin, $C_{51}H_{98}O_6$ (mol/mol)	0.265
Triolein, $C_{57}H_{104}O_6$ (mol/mol)	0.455
Trilinolein, $C_{57}H_{98}O_6$ (mol/mol)	0.128
Glycerol-tristearate, $C_{57}H_{110}O_6$ (mol/mol)	0.152

The characteristics of the microbial oil feed stream were obtained from D6.2 [2] and are presented in Table 23 while the basic specifications for the overall unit are summarized in Table 24. The reactors operating parameters were obtained from D5.4 [22]. For the separate retrieve of medium and heavy kero, the heavy fraction is obtained from stage 20 in liquid form with a flow ratio of 0.24 (mass basis). The reactor dimensions and designs that are taken into consideration at the HDR-02 model are L=0.954m, D=27.94mm and 0.326 kg catalyst loading (2300 kg/m^3 density).

Table 24. Thermocatalytic part process specifications (main case)

parameter	value
Oil pump pressure outlet (bar)	103.42
H_2/oil feed ratio	5000 scfb or 0.0833 kg/kg
Oil inlet temperature at Reactor 1 (ºC)	270
Reactor 2 outlet temperature (ºC)	340
Reactor 2 pressure drop (kPa)	15
Flash operation (ºC/bar)	45/ 96.26
Decanter operation (ºC/bar)	25/ 7.093
Hydrogen recovery/purity at PSA	93%/100%
Column 1 number of stages	4
Column 1 condenser pressure (bar)	1.11
Column 1 feed stage number	2
Column 2 inlet pressure (bar)	4.05
Column 2 number of stages	22
Column 2 condenser pressure (bar)	1.11
Column 1 feed stage number	11

5.1.2 Model validation

At first, the model validation is assessed against the pilot campaign data. The model was set according to the TRL5 reactor size and the inlet gas streams and the simulation results were compared against the respective pilot results. Graphs in Figure 37 shows the comparison of these results.

Table 25. Gas product composition analysis measured from pilot runs

component	Molar fraction (% v/v)
Hydrogen	94.28008
Propane	1.960729
C6+ hydrocarbons	0.007105
N-butane	0.018067
Isopentane	0.003847
N-pentane	0.003788
Nitrogen	0.077232
Hydrogen Sulfide	0
Methane	0
Ethane	0
Carbon dioxide	0
Carbon monoxide	0

As seen in Figure 37, the model is able to predict in good agreement not only the fractions of the main product streams but also the particular liquid fuel fractions after refining. Regarding the gas streams, there is an over-prediction in propane and the model foresees steam at the gas stream after the flash separation, whereas it is not detected in gas measurements. Overall, the model enable us to proceed with the scale up and the dynamic simulations.

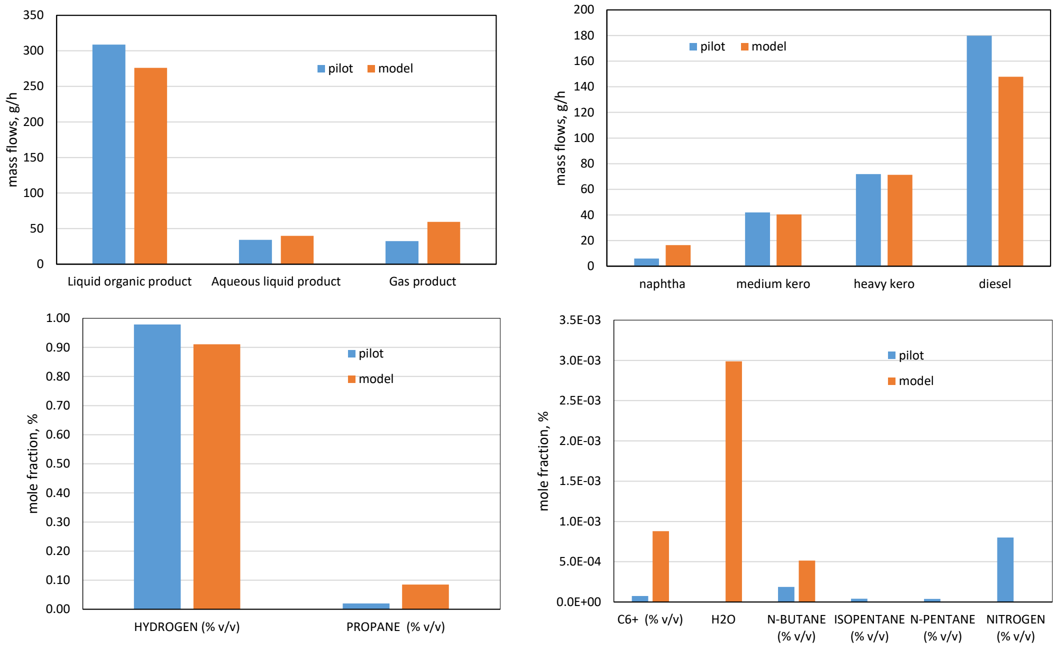

Figure 37. Comparison of measured and model predicted product results for pilot scale

For the model upscaling at full scale, given the input data of initial oil feed stream flow rate, a scale factor of 18000 is considered and applied for the increase of reactor 2 dimensions and catalyst loading.

5.2 Control strategy and investigated scenarios

The focus of the control strategy of this unit is given to the maintenance of the desired specifications at the reactors (H_2/oil ratio at the inlet, temperature), separation vessels (flash, decanter and columns) temperatures that will secure stable and consistent fuels production and retrieval despite ‘disturbances’ (e.g. oil flow ramp up/down).

Dedicated PI controllers have been applied for: (Figure 38)

- Maintenance of hydrogen concentration at reactor inlet (0.9728) via regulating the makeup hydrogen flow
- Maintenance of kerosene main specifications like boiling temperature (180 °C) via column 2 condenser duty regulation
- Maintenance of cooling steam temperature outlet from the reactors (400 °C) via flow control

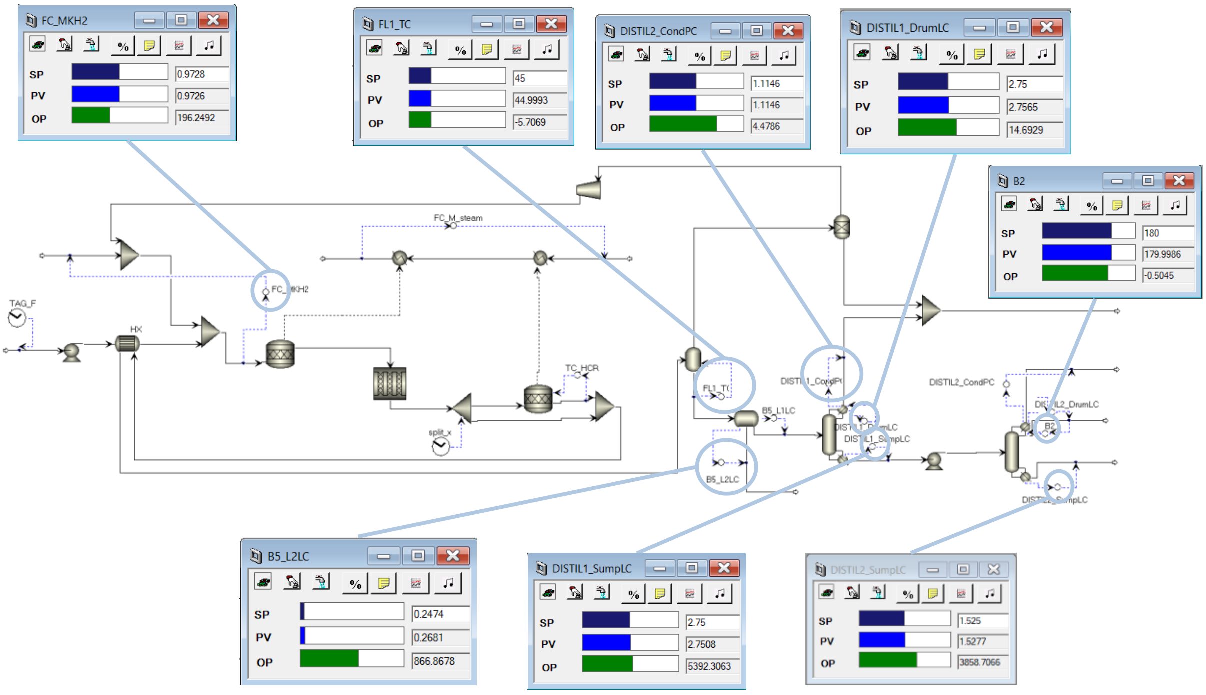

FC_MKH2
SP 0.9728
PV 0.9726
OP 196.2492

FL1_TC
SP 45
PV 44.9993
OP -5.7069

DISTIL2_CondPC
SP 1.1146
PV 1.1146
OP 4.4786

DISTIL1_DrumLC
SP 2.75
PV 2.7565
OP 14.6929

B2
SP 180
PV 179.9986
OP -0.5045

B5_L2LC
SP 0.2474
PV 0.2681
OP 866.8678

DISTIL1_SumpLC
SP 2.75
PV 2.7508
OP 5392.3063

DISTIL2_SumpLC
SP 1.525
PV 1.5277
OP 3858.7066

Figure 38. APD oil hydroprocessing and main controllers setup

The following table summarizes the scenarios and the respective control strategies that are going to be investigated at dynamic/unsteady conditions:

Table 26. Examined scenarios and the control strategy (tentative)

a/a	Disturbance/change	Target	Variable parameter(s)
1	Change in TAG flow rate	Final products main specs	Make-up H2 flow, cooling water flow, column 2 condenser duty
2	HCR reactor by-pass flow rate changes		

The fist scenario is associated with the disturbance that plant operation load drops below its design point and the reduced amount of microbial oil enters the hydrotreatment unit. In the second one, the ability of the unit to operate flexibly when the operator wish to modify (increase) the diesel/jet fuel ratio, by reducing the amount of hydrocarbons that undergo hydrocracking and hydroisomerization.

5.3 Dynamic process simulations

5.3.1 TAGs flow rate variation

As seen in Figure 39a, the crude hydrotreated oil follows the trend of oil flow change, and the stability in the updated flow rate is restored in a very short time (a few minutes) after each step change. This fact verifies that the reactors system and the gas/liquid separation unit (including water removal) have a very robust control system that restores very quickly at the desired conditions according to the set points. Interestingly, the hydrogen supply operate in an effective way and the total hydrogen flow rate at the reactor inlet has similar behavior with the produced bio-crude (Figure 39b). The reactors temperatures are not perfectly closed to the set point temperatures (340 ºC) as depicted in Figure 39c but no considerable deviation is detected. On the other hand, the control system in Column 2 fail to keep it at a desired operation framework and the jet fuel production is eliminated after the first step change (Figure 39a). The jet fuel steam is appeared again at t=4.5 h but could not reach a stable condition again as the initial bio-crude feed drops by 20%. What is inferred is that that column can operate normally only at the design point under the given control strategy. Moreover, the temperature and pressure outlet of the jet fuel stream did not remain stable during the whole process but the jet fuel yield starts varying even when temperature and pressure were close to the respective set points.

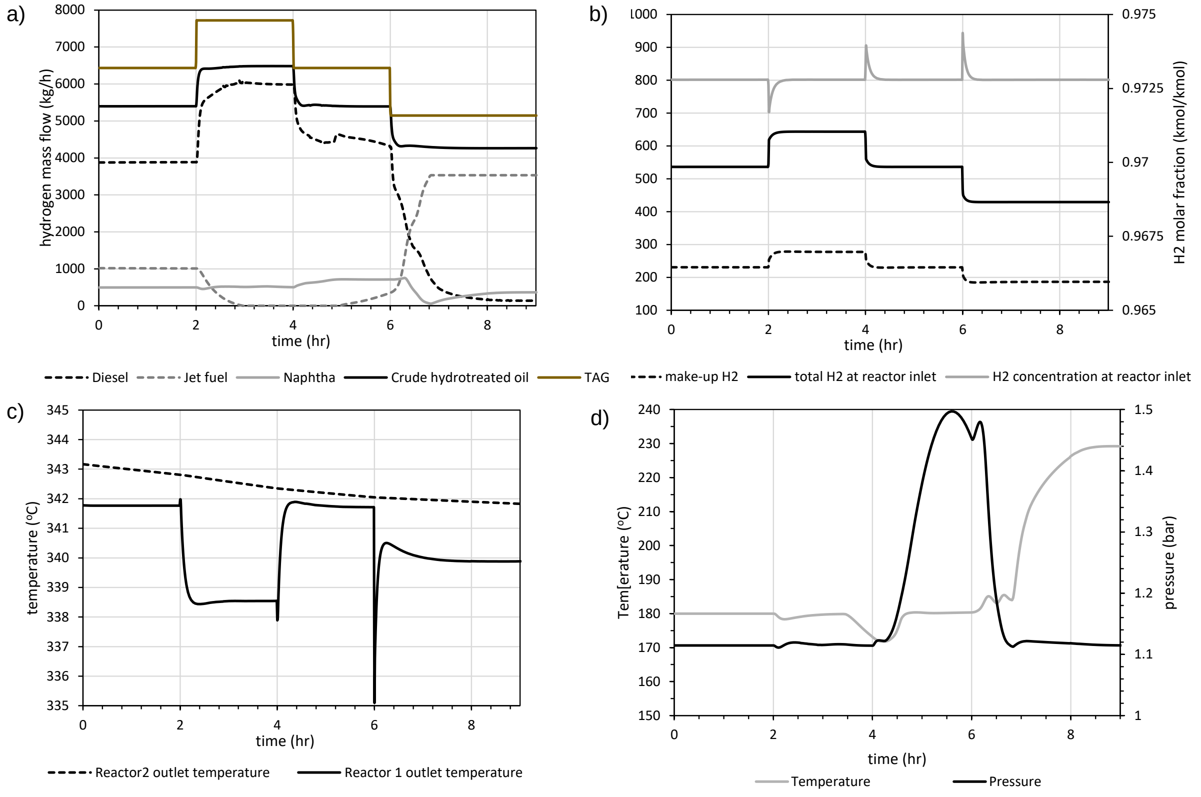

Figure 39. Main process outputs behavior at sudden drops in oil flow rate

5.3.2 Bypass at Hydrocracker reactor

When the bypass stream flow increases and the inlet flow at Reactor 2 drops (Figure 40a), the diesel yield linearly increases as less long chain hydrocarbons are broken into smaller one (Figure 40b). On the other hand, naphtha flow remains almost stable and the restricted hydrocracking reactions have impact merely on the jet fuel fraction. Contrary to the previous case, column 2 operates at the desired set point as concerns the jet fuel specified temperature and pressure (Figure 40c). It is easily concluded that the present control at the second distillation column works effectively at variable conditions provided that the inlet flow rate remains stable and at the design point. Finally, the behavior at the make-up hydrogen flow and the specified H_2 concentration at the reactor inlet is quite expectable and according to the initial control strategy (Figure 40d).

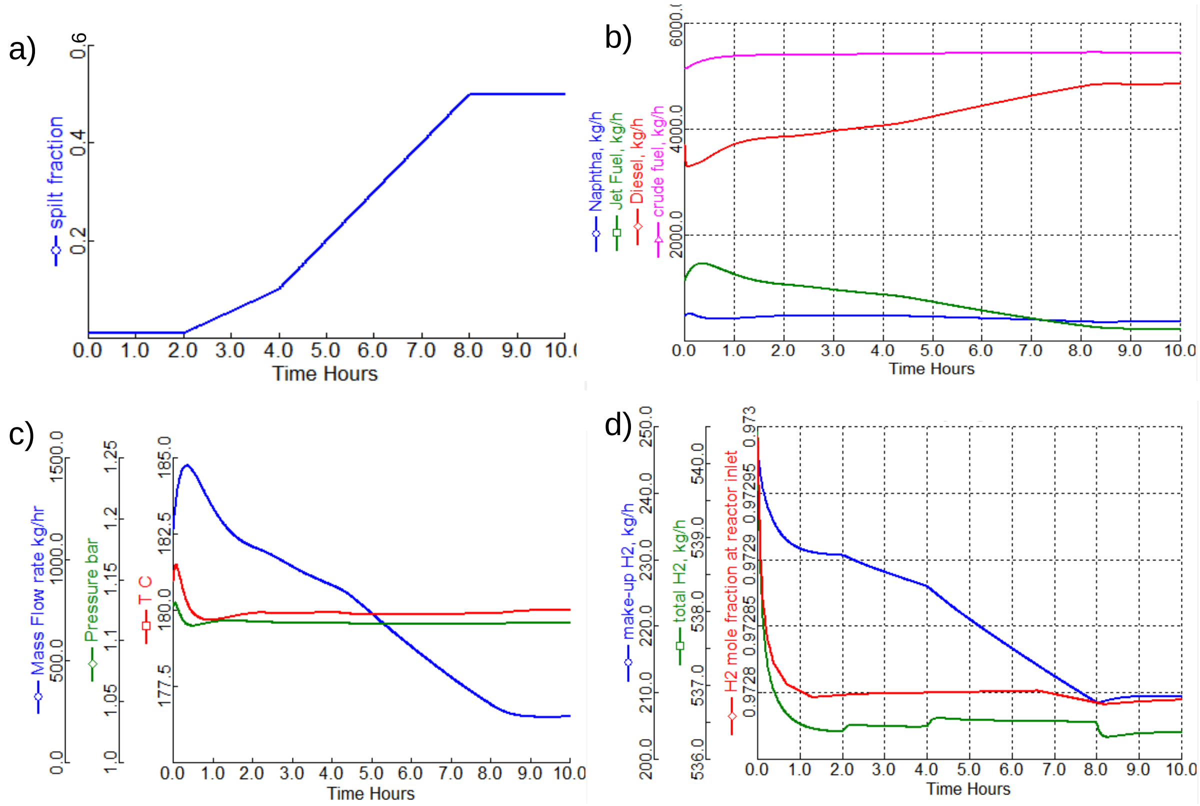

Figure 40. Main process outputs behavior when decreasing the inlet stream at hydrocracker (reactor 2)

6 Conclusions

The key conclusions that are derived from the Task 6.4 activities are summarized below.

Thermochemical part: While the reactors temperatures maintained at the desired levels, the H_2/CO increased when the feedstock flow rate decreased. Changes in the gasifier temperature can be handled and the process performance can be restored and maintained at the initial specifications through the appropriate control of the circulating solids flow rate. Variations in the water/steam flow and external gas that burnt in the oxidizer affect the stability of the syngas composition and a difference control strategy approach should be adopted in case that the different H_2/CO ratio has negative impact on the gas fermentation performance and cannot be restored at the desired levels after the ATR.

Biological Part: In the syngas fermentation process, variations in syngas composition were considered, prompting the testing of various scenarios involving CO, CO_2 and H_2 to control the acetate production by fine-tuning agitation speed. Hydrogen variations found to notably influence agitation speed, while the impact of CO was comparatively minor. In the acetate fermentation process, fluctuations in acetate concentration and liquid flow rate are exhibited, often attributed to potential malfunctions in the syngas fermentation controllers. To counteract this, the controlled system primarily focuses on optimizing the lipid production phase. By maintaining acetate residuals close to zero, and ensuring satisfactory TAGs production, biomass concentration was adjusted accordingly. Adjusting biomass concentration produced in the growth phase is crucial for achieving desired final product outcomes and residuals. This adjustment involves optimizing operational parameters during the growth phase, such as agitation speed, oxygen flow and C/N ratio. While this task is not executed in this deliverable, it was studied that other operational parameters in the lipid production phase, such as agitation speed and oxygen flow rate exert a smaller influence on final acetate concentration compared to biomass concentration.

Thermocatalytic part: The fuel production and bio-crude recovery part that consists the reactors and the gas/liquid separation step has a good behaviour and stability at the process specifications when the operation load (oil flow rate) or the diesel/jet fuel ratio set-point change. The proper control of the make-up hydrogen and the temperature at both reactors has been accomplished, achieving thus a smooth operation of the reactors that led to the expected oil to hydrotreated TAGs conversion. On the other hand, the second column operated improperly at lower loads, failing to separate the bio-jet fraction and under the specified condenser temperature. More effort should be paid in order to setup a robust control of the distillation column to secure its proper operation when lower smaller bio-crude flow rate is fed. When the by-pass fraction variation at the second reactor was examined, no similar issues were observed although the feed composition varied.

7 Future work and outlook

There is still some room for improvement of the DFBG dynamic model, especially focusing on the better prediction of solids distribution along the riser and the inclusions of hydrodynamics and reactions at the oxidizer. Moreover, other parts like the loop seal the connection duct between the two reactors for an improved illustration of the hydrodynamics and solids in the system could be considered. Last but not least, the inclusion of the tars reforming at the autothermal reformer should be performed in a follow-up study to verify whether the syngas composition can be regulated there.

Integration of energy balances in both syngas and acetate fermentation processes could be executed in the models, focusing on examining the influence of cooling water supply in maintaining the reaction temperature and its impact on variations in the syngas or acetate composition. Further efforts will be directed towards refining the control of biomass concentration during the growth phase through adjustments in operational parameters, as previously analyzed. Additionally, ongoing improvements in PID coefficients for the syngas fermentation process are anticipated, with the goal of achieving a faster steady-state condition to enhance process efficiency and stability. This future work will contribute to advancing the understanding and control of these fermentation processes for improved acetate and lipid production.

Finally, at the thermocatalytic section, the control strategy at the second distillation column should be improved when the feed stream flow rate drops. Moreover, a more detailed reactor modeling especially on the reactions associated to the hydrocracking and hydroisomerization, depending on what data are available from the respective real tests, would lead to fuel products with advanced properties. In that case, a better evaluation on their specifications would be carried out. Furthermore, an analytical modeling on the hydrogen recovery before its recirculation is scheduled as a future work.

8 References

[1] Mohammad Ghazani and, Stamatopoulos P. Deliverable D6.1 Report on DFB Gasification Modelling. 2023.

[2] Maragkoudaki, Leda; Detsios N, Atsonios K. Deliverable 6.2 Results of full-chain process simulations. 2023.

[3] Detsios, Nikos; Maragkoudaki, Leda; Atsonios K. D2.5 Full process basic definition. 2021.

[4] Myöhänen K, Palonen J, Hyppänen T. Modelling of indirect steam gasification in circulating fluidized bed reactors. Fuel Process Technol 2018;171:10–9. https://doi.org/https://doi.org/10.1016/j.fuproc.2017.11.006.

[5] Petersen I, Werther J. Experimental investigation and modeling of gasification of sewage sludge in the circulating fluidized bed. Chem Eng Process Process Intensif 2005;44:717–36. https://doi.org/https://doi.org/10.1016/j.cep.2004.09.001.

[6] Lasheras A, Ströhle J, Galloy A, Epple B. Carbonate looping process simulation using a 1D fluidized bed model for the carbonator. Int J Greenh Gas Control 2011;5:686–93. https://doi.org/https://doi.org/10.1016/j.ijggc.2011.01.005.

[7] Kunii D, Levenspiel O, Brenner H. Fluidization Engineering. Elsevier Science; 1991.

[8] Pauls JH, Mahinpey N, Mostafavi E. Simulation of air-steam gasification of woody biomass in a bubbling fluidized bed using Aspen Plus: A comprehensive model including pyrolysis, hydrodynamics and tar production. Biomass and Bioenergy 2016;95:157–66. https://doi.org/https://doi.org/10.1016/j.biombioe.2016.10.002.

[9] Ohlemüller P, Alobaid F, Gunnarsson A, Ströhle J, Epple B. Development of a process model for coal chemical looping combustion and validation against 100kWth tests. Appl Energy 2015;157:433–48. https://doi.org/https://doi.org/10.1016/j.apenergy.2015.05.088.

[10] Mori S, Wen CY. Estimation of bubble diameter in gaseous fluidized beds. AIChE J 1975;21:109–15. https://doi.org/https://doi.org/10.1002/aic.690210114.

[11] Gilliland ER. Fluidised particles, J. F. Davidson and D. Harrison, Cambridge University Press, New York (1963). 155 pages. $6.50. AIChE J 1964;10:783–5. https://doi.org/https://doi.org/10.1002/aic.690100503.

[12] Karmakar MK, Datta AB. Hydrodynamics of a dual fluidized bed gasifier. Adv Powder Technol 2010;21:521–8. https://doi.org/https://doi.org/10.1016/j.apt.2010.02.001.

[13] Kaiser S, Löffler G, Bosch K, Hofbauer H. Hydrodynamics of a dual fluidized bed gasifier. Part II: simulation of solid circulation rate, pressure loop and stability. Chem Eng Sci 2003;58:4215–23. https://doi.org/https://doi.org/10.1016/S0009-2509(03)00233-1.

[14] Trevethick SR, Bromley JC, Waters GW, Koepke M, Tran LP, Overgaard RJ. Multi-Stage Bioreactor Process 2016;1:1–21.

[15] Atlić A, Koller M, Scherzer D, Kutschera C, Grillo-Fernandes E, Horvat P, et al. Continuous production of poly([R]-3-hydroxybutyrate) by Cupriavidus necator in a multistage bioreactor cascade. Appl Microbiol Biotechnol 2011;91:295–304. https://doi.org/10.1007/s00253-011-3260-0.

[16] Deliverable 3.4 Optimization of syngas fermentation process parameters for acetic acid production (1st stage). n.d.

[17] Deliverable 3.5 Optimization of acetate fermentation process parameters for C14 and C16-18 TAGs production (2nd stage). n.d.

[18] de Medeiros EM, Posada JA, Noorman H, Filho RM. Dynamic modeling of syngas fermentation in a continuous stirred-tank reactor: Multi-response parameter estimation and process optimization. Biotechnol Bioeng 2019;116:2473–87. https://doi.org/10.1002/bit.27108.

[19] Fermentor B. BioFlo 4500 Benchtop Fermentor / Bioreactor. 2002.

[20] Béligon V, Poughon L, Christophe G, Lebert A, Larroche C, Fontanille P. Validation of a predictive model for fed-batch and continuous lipids production processes from acetic acid using the oleaginous yeast Cryptococcus curvatus. Biochem Eng J 2016;111:117–28. https://doi.org/10.1016/j.bej.2016.01.016.

[21] Pan W, Wu JH, Li LF, Liu HM, Li Q. The research of pid control in a large scale helium refrigerator. IOP Conf Ser Mater Sci Eng 2015;101. https://doi.org/10.1088/1757-899X/101/1/012172.

[22] Dimitriadis, Athanasios; Bezergianni S. Deliverable D5.4 Validation of TAG upgrading technology in industrially-relevant scale. 2024.

[23] Arora P, Grennfelt EL, Olsson L, Creaser D. Kinetic study of hydrodeoxygenation of stearic acid as model compound for renewable oils. Chem Eng J 2019;364:376–89. https://doi.org/https://doi.org/10.1016/j.cej.2019.01.134.

[24] Castagnari Willimann Pimenta JL, de Oliveira Camargo M, Belo Duarte R, Andreo dos Santos OA, de Matos Jorge LM. A novel kinetic model applied to heterogeneous fatty acid deoxygenation. Chem Eng Sci 2021;230:116192. https://doi.org/https://doi.org/10.1016/j.ces.2020.116192.

[25] Tirado A, Ancheyta J, Trejo F. Kinetic and Reactor Modeling of Catalytic Hydrotreatment of Vegetable Oils. Energy & Fuels 2018;32:7245–61. https://doi.org/10.1021/acs.energyfuels.8b00947.

[26] Martinez-Hernandez E, Ramírez-Verduzco LF, Amezcua-Allieri MA, Aburto J. Process simulation and techno-economic analysis of bio-jet fuel and green diesel production — Minimum selling prices. Chem Eng Res Des 2019;146:60–70. https://doi.org/https://doi.org/10.1016/j.cherd.2019.03.042.

Annexes

The gas-liquid equilibrium factors for non-condensable and condensable for components in syngas fermentation are listed in Table 27.

Table 27: Gas-liquid equilibrium factors for syngas fermentation

Component	$m_{j,NC}, m_{j,C}$
CO	34.94382192
CO_2	0.846888685
H_2	47.03219153
HAc	10045.22035
H_2O	22729.31687
NH_3	0.001110794
H_2S	0.582181961
HCN	0.005966242
COS	2.656746587
Benzene	0.295439135

The mass diffusivity of species j in water, $D_{f,j}$ in syngas fermentation process are listed in Table 28.

Table 28: Mass diffusivity of components in water for syngas fermentation

Component	$D_{f,j}\left(\frac{cm^2}{sec}\right)$
CO	0.0000203
CO_2	0.0000192
H_2	0.000045
HAc	0.0000099
H_2O	0.000000002299
NH_3	0.000024
H_2S	0.0000161
HCN	0.0000203
COS	0.0000159
Benzene	0.0000109
Air	0.00002

The gas-liquid equilibrium factors for components in acetate fermentation are listed in Table 29:

Table 29: Gas-liquid equilibrium factors for acetate fermentation

Component	m_j
CO	0.5472
O_2	0.2145
CO_2	0.000606
Acetate	9786.3

The mass diffusivity of species j in water, $D_{f,j}$ in acetate fermentation process are listed in Table 30.

Table 30: Mass diffusivity of components in water for acetate fermentation

Component	$D_{f,j}\left(\frac{cm^2}{sec}\right)$
CO_2	0.0000192
O_2	0.0000210
Air	0.00002

The fitted parameters for syngas fermentation for the studied cases are shown in Table 31 .

Table 31: Fitted parameters for syngas fermentation

Parameter	Fitted to the experimental data from D3.4 [16]	Fitted to the experimental data from T4.3	Fitted to industrial scale data from D6.2 [2]
klaHAc	3000.5	5.3	-
klaCO	2607.84	2585.64	-
$klaH_2$	3865.40	3865.4	-
$klaCO_2$	3078.07	3078.06	-
$klaH_2O$	34.78	34.5	-
vmaxco	0.022	0.022	10.505
vmaxh2	0.015	0.015	15.893
Ksco	0.0009	0.0009	0.0035
Ksh2	0.00021	0.00021	0.008
KIHAc	0.1	0.1	5.704
KIco	0.000136	0.000136	1.121
Yxco	3.6434	3.643	5.14
Yxh2	1.976	70.74	17.08
kd	0.011	0.05	0.26
KInh3	-	1.325	0.409
KIh2s	-	1.742	1.879
KIhcn	-	2.6	2.6
KIcos	-	1.519	1.519
KIbenzene	-	0.984	1.298

Yacco	-	4	0.7
Yach2	-	22.62	1.279
klanh3	-	500.399	-
klah2s	-	10	-
klahcn	-	9.999	-
klacos	-	10	-
klabenzene	-	10	-
f0	-	-	0.89
Agitation Speed	-	-	25

The dynamic profile of biomass, acetate, CO, H_2, CO_2 concentrations after parameter fitting during syngas fermentation are illustrated in Figure 41, Figure 42 and Figure 43 for the experimental data from D3.4 [16] (cleaned syngas) and T4.3 (syngas with impurities).

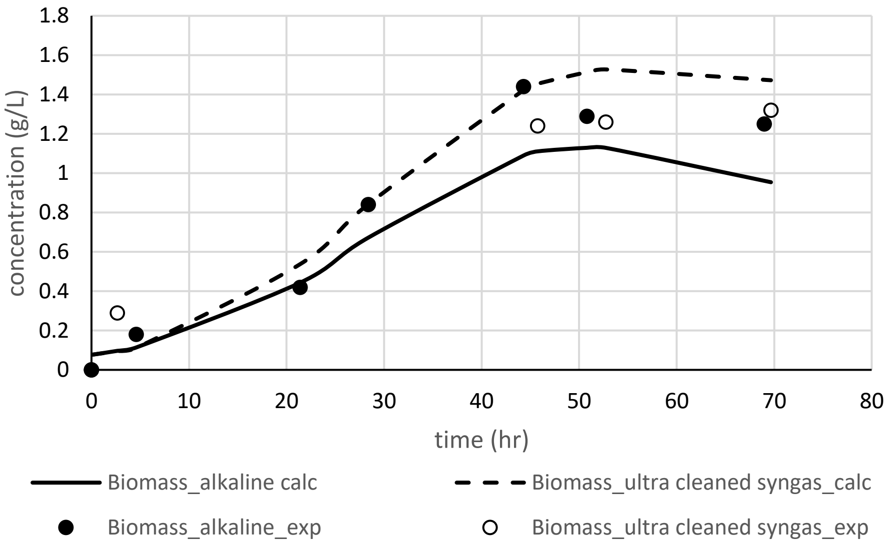

Figure 41: Dynamic profile of biomass for experimental data from D3.4 [16] *and T4.3*

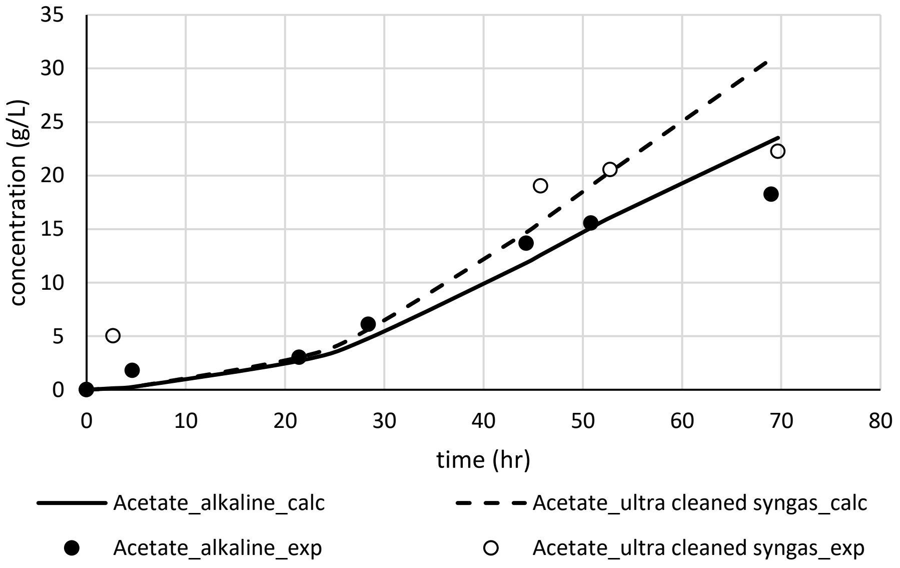

Figure 42: Dynamic profile of acetate production for experimental data from D3.4 [16] *and T4.3*

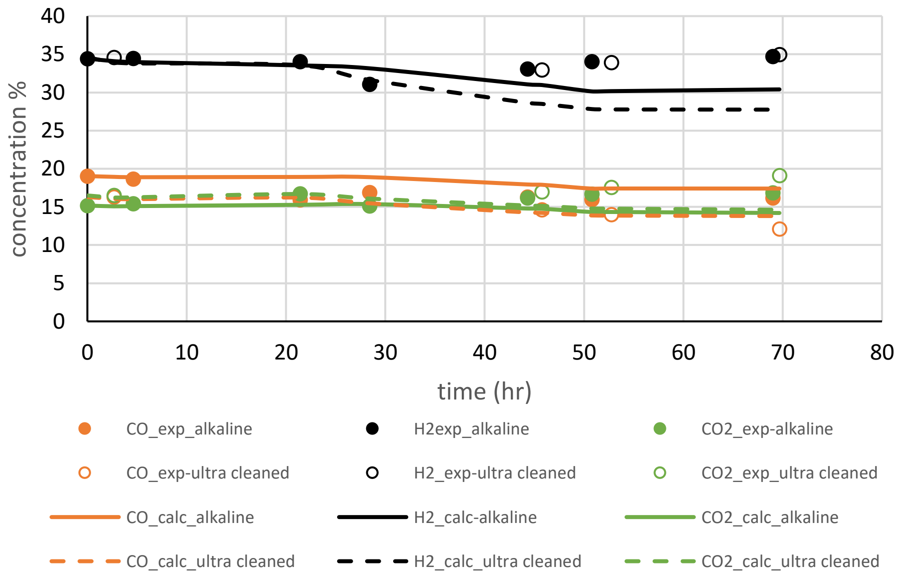

Figure 43: Dynamic profile of CO, H_2, CO_2 consumption after parameter fitting in experimental D3.4 [16] *data*

Upon analysis of Figure 41. Figure 42 and Figure 43 it is evident that the biomass and acetate production rates vary depending on the inclusion of impurities in the initial feedstock. As for the acetate fermentation, the fitted parameters for the studied cases are shown in Table 32.

Table 32: Fitted parameters for acetate fermentation

Parameters	Fitted to the experimental data from D3.5 [17]	Fitted to the industrial scale data from D6.2 [2]	
	Lipid phase	**Growth phase**	**Lipid phase**
μ_{max}	4.975	12000000	-
K_s	9.9802	1	0.000002
K_{SN}	0.82	0.9105852	0.18585
K_{SO2}	2.934	0.1216647	0.000055
B	1.656	0.3	50.139998
I_1	0.57	-	0.7
Y_{Xac}	2.0764	0.4	0.0000000002
m	0.243	0.2	550
I_2	0.11	0.1	0.1
Y_{XO2}	3.487	5.8925	0.892497
Y_{XN}	92.399	9.08	0.00000058
K_{s1}	2.016	-	66.35077
K_{s2}	3.673	-	0.45390
K_{s3}	0.10	-	0.539029
μ_{max1}	1	-	2.127215
f_0	-	0.9988244061	0.998824
kla_{O2}	64.34856	-	-
Y_{lac}	50.63	0.0855011432	0.008550
Y_{xCO2}	-	0.50	0.0000000005
k_d	0.0099415	-	-
Agitation speed	-	30	30

The $K_{s1}, K_{s2}, K_{s3}, \mu_{max1}$ parameters are the equivalent $K_s, K_{SN}, K_{SO2}, \mu_{max}$ parameters used in the R_X equation during the lipid production phase.

The dynamic response of acetate, CDW (Cell Dry Weight) and TAGs concentrations during acetate fermentation after parameter fitting with the experimental data from D3.5 [17] is illustrated in Figure 44.

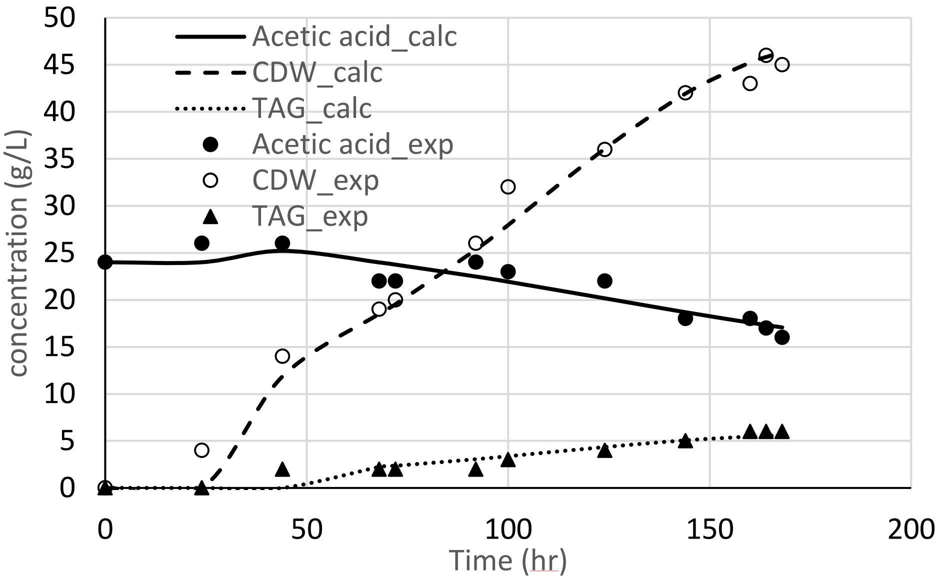

Figure 44: Predicted dynamic profiles of acetate, TAGs and CDW and experimental points for D3.5 [17]

Upon analysis of Figure 44 it is evident that the model parameters accurately describe the acetate, TAGs and CDW concentration profiles.